MSc thesis in Applied Physics

Graphene gas sensor

Ireneusz Eugeniusz Rosłoń

2018

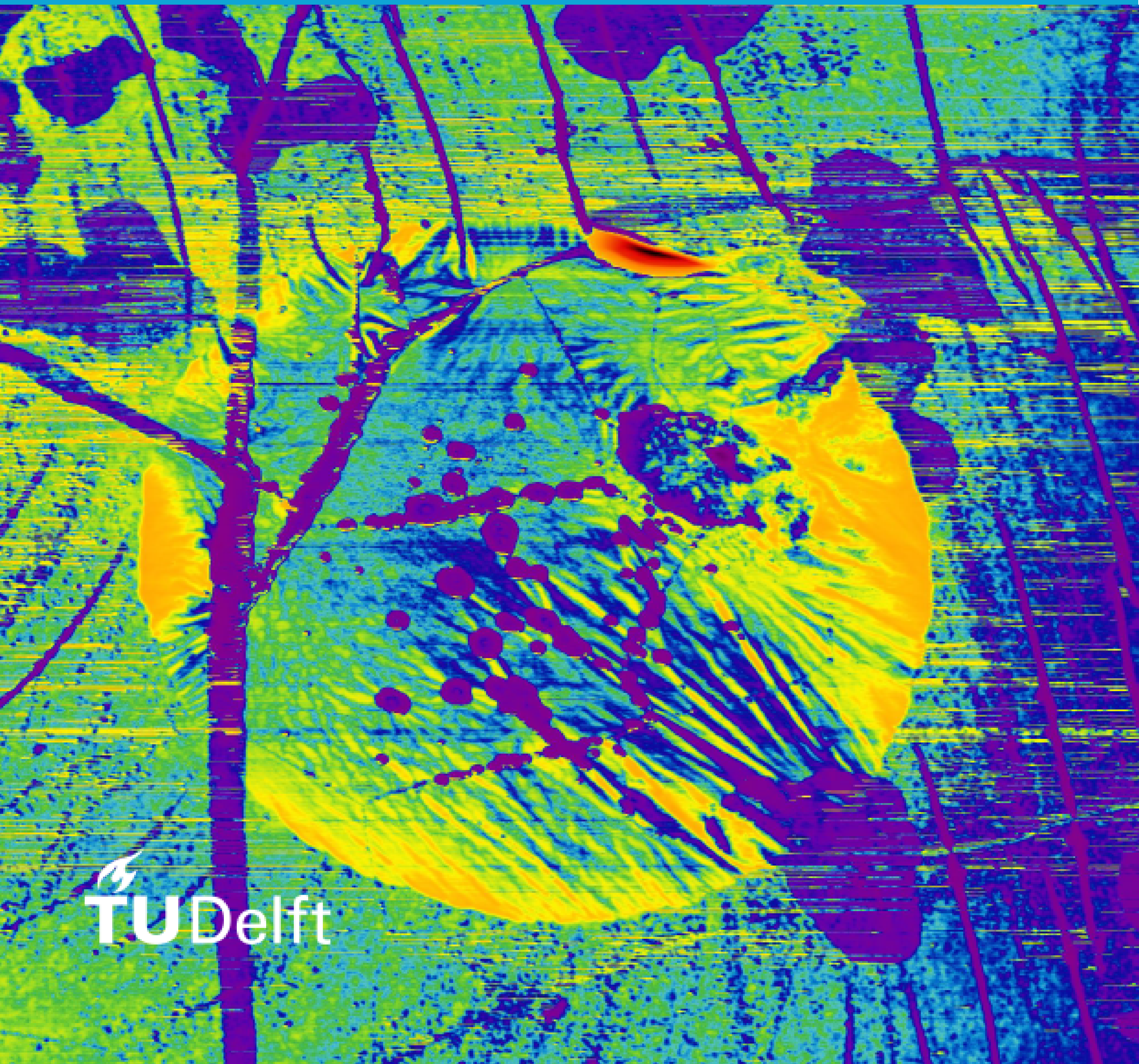

GRAPHENE GAS SENSOR

A thesis submitted to the Delft University of Technology in partial fulfillment
of the requirements for the degree of

Master of Science in Applied Physics

by

Ireneusz Eugeniusz Rosłoń

July 2018

Ireneusz Eugeniusz Rosłoń: *Graphene gas sensor* (2018)
An electronic version of this thesis is available at
`http://repository.tudelft.nl/`

The work in this thesis was made in the:

Steeneken Lab of Applied Nanophysics
Department of Quantum Nanoscience
Faculty of Applied Science
Delft University of Technology

Thesis committee:	Prof. dr. P.G. Steeneken
	Prof. dr. F. Alijani
	Prof. dr. H.S.J. van der Zant
Daily supervision:	Ir. R.J. Dolleman

ABSTRACT

Gas permeation through graphene membranes has received considerable attention for water purification and molecular sieving applications. However, characterization of the permeation has been limited to long timescales of minutes. This thesis shows a method for measuring gas permeation through porous graphene membranes at the microsecond timescale. Suspended porous graphene membranes, with an average pore size of 14 nm and a single 400 nm pore, are brought into sinusoidal motion by optothermal actuation. By monitoring the frequency dependent phase delay between actuation signal and mechanical motion, the gas dependent permeation time of the porous membrane is determined. The permeation time constant is demonstrated to be proportional to the square root of the molecular mass, indicating an effusion dominated permeation mechanism. The determination of permeation at timescales below 1 μs using a femtoliter gas cavity opens up opportunities for novel nanoscale porous graphene based gas sensors, with very fast response times.

PREFACE

If this be error and upon me prov'd,
I never writ, nor no man ever lov'd.
– W. Shakespeare

Reflections on graphene — the phrase I believe is most appropriate to condense the true nature of this thesis. It represents the many thoughts that have been given to the topic in the course of countless discussions, the long experimenting and the writing. At the same time it hints to what was observed in fact: the light reflected from a tiny area of graphene. Showing in this way a glimpse of the bending, heating, flowing and moving, taking place on a scale otherwise obscure.

In a manifold of observables and unknowns it is of the greatest worth to have a guiding voice near. For that I thank my direct supervisors and my lab comrades. Robin and Peter, for making me look farther than my gaze would allow for. Martin, Mick, Makars and Dejan, being truly comrades in the field. My thesis committee and staff, for putting time and effort into this work. My fellow peers and students with whom I shared the experience of writing a thesis. And finally I would like to thank my Króliczek, my mum and my dad for patiently listening to my ever continuing stories on membranes.

A last word on the citation. In no case I would dare to state that my work is flawless. The true-truth is that it has been put onto paper with enthusiasm and fervor, as result of a year of passionate work. I hope you, the reader, will find that passion too.

Irek Rosłoń

Delft,
July 13, 2018

CONTENTS

1 INTRODUCTION 3
1.1 Graphene nanodrums 3
1.2 Nanoporous sieving 4
1.3 Outlook 4

2 THEORY 5
2.1 The harmonic oscillator 5
2.2 Sinusoidally driven oscillator 6
2.3 Damping 7
2.3.1 Thermoelastic damping 7
2.3.2 Akhiezer damping 7
2.4 Phase 7
2.5 Impact of defects 8
2.5.1 Young's modulus 9
2.5.2 Density 9
2.5.3 Stress 9
2.5.4 Grain boundaries 9
2.6 Gas flow 9
2.6.1 Continuum flow 10
2.6.2 Classical effusion 11
2.6.3 Molecular sieving 11

3 METHODS 13
3.1 Interferometry setup 13
3.2 Actuation 13
3.3 Read-out 13

4 CHARACTERIZATION 15
4.1 An unperforated nanodrum 15
4.2 Gas permeation sample 1 15
4.3 Gas permeation sample 2 17
4.4 Mechanical characterization 18

5 GAS PERMEATION MODEL 21
5.1 Model summary 21
5.2 Gas pressure inside cavity 22
5.3 Pressure - deflection relation 23
5.4 Full model derivation 24
5.5 Equivalent electric model 25
5.5.1 Thermal 25
5.5.2 Mechanical domain 25
5.5.3 Pneumatic domain 26
5.6 Electric model simulation 27
5.6.1 Numerical values 27
5.6.2 Simulation results 28

6 RESULTS 31
6.1 Typical response 31
6.1.1 Time constants 31

6.1.2 Coefficients 32
6.2 Measurements 32
6.3 Thermal time constant 33
6.4 Comparison with vacuum 36

7 CONCLUSION AND DISCUSSION 37
7.1 Gas permeation model 37
7.2 Recommendations 38

A TABLES 43

1 INTRODUCTION

The unique physical characteristics of suspended sheets of graphene are promising for realizing novel sensors.[1] Graphene is an ultimately thin material consisting of only one layer of carbon atoms. Its atomic thickness makes it a perfect example of a 2D material, whose physics can be simplified to that of a flat sheet. Not only is graphene one atom thick, it is also the strongest material known.[2] In theory, a sheet of graphene of one square meter is strong enough to support a cat laying on it. Together with its particular electrical properties,[3] this material is outstanding for use in next-generation electronics and sensors.

While pristine graphene is impermeable for all gasses and liquids, perforations cause selective permeability which can be adapted for filtration, separation and chemical sensing purposes.[4–7] Bombardment with swift heavy ions to form nanometer sized pores has been proved successful in functionalizing graphene membranes for these purposes.[8,9] Theoretical studies predict that perforating graphene with nanometer sized pores leads to molecular sieving, allowing for unprecedented selectivity.[10] However, the detection of the permeability of such membranes is limited to large timescales, as it is relaying on devices with long response times like flow and pressure meters.[11] This thesis demonstrates a fast, low-power and miniaturizable device for detecting gasses using perforated graphene membranes. The principle of operation is based on the distinct effusion rates of gasses, deriving from differences in molecular mass and particle velocity.

1.1 GRAPHENE NANODRUMS

Microsized devices generally profit from low cost of production, low power consumption, high portability and low environmental impact. These advantages very well agree with current needs for innovation. Recent progress in micro- and nanomechanical systems (MEMS and NEMS) is visible in readily available applications as accelerometers,[12] mass sensors,[13] pressure meters[14] and RF devices.[15] The configuration of graphene nanodrum, first reported in 2008,[16] is applied in this thesis for gas sensing purposes.

A nanodrum is an equivalent of a percussion drum on the nanoscale. Several pictures from recent work on nanodrums are shown in figure 1.1. The graphene is suspended over a cavity and can be brought into motion by electrical or optical impulses. In the last years research has been focusing on understanding the physics of these devices, arriving at beautiful results such as the experimental displacement mapping of a vibrational mode.[17] The next step is finding commercialisable applications of the nanodrums. Perforated graphene sheets are investigated for their capabilities in water

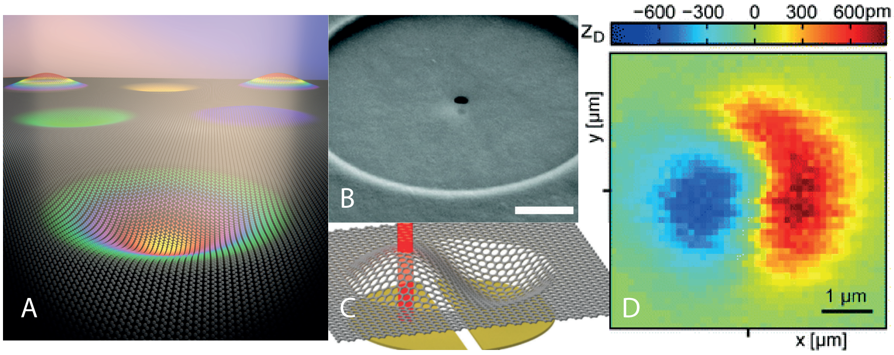

Figure 1.1: Pictures taken from recent work on graphene.[16–19] A) Artist impression of graphene nanodrums. B) SEM image of a graphene drum with a milled nanopore with scalebar 1 μm. C) Excitation of the second mode of a circular membrane is either performed by electric gating or laser actuation. D) Measured displacement map of a graphene membrane using laser interferometry.

purification and separation of substances in general, promising to outperform existing devices.

1.2 NANOPOROUS SIEVING

Nanoporous materials allow for unprecedented separation of substances with both high selectivity and throughput. A first account on filtration using nanoporous graphene is given by Celebi et al., who discusses permeation through pores ranging from 10 nm to 1000 nm. The small dimensions of the pores are beneficial for selectivity, as the differences in atomic structure become a dominant factor for selectivity at the small scale. Usually, perforations are created using a focussed ion beam, but recent development works toward more versatile and general approaches for bombardment of large areas.[20] Selective transport of gasses has been shown for H_2/CO_2, H_2/N_2 and N_2/CO_2 using graphene oxide membranes.[21] For perforated graphene membranes the permeation speed of a range of gasses (H_2, CO_2, Ar, N_2, CH_4 and SF_6) has been shown to depend on the mass of the gas.[22] Similar permeation mechanisms are investigated in this thesis.

1.3 OUTLOOK

This thesis is the account of nearly one year of work towards understanding, modeling and measuring gas permeation through porous graphene. The reader is first introduced to the theory and the model describing the mechanics of a perforated graphene membrane in motion, after which the surface characteristics of the nanodrums are discussed. Then, the vacuum measurements are presented, showing the influence of perforations onto the mechanics. Finally, the measurements in gaseous environment are discussed. The frequency responses of the drums are used to distinguish the various gasses, thereby demonstrating a gas sensing device making use of perforated graphene membranes.

2 THEORY

The theory section aims to give a brief and insightful summary of physical concepts used in this thesis. It is by no means a comprehensive story, like the ones found in school books, but intends to be a good introduction to the models presented in the following chapters. It starts with describing the motion of a harmonic oscillator. The concept of phase is given its own section, since phase detection lays at the heart of the measurements performed in this thesis. Finally, this chapter ends with an overview on the theory of gas permeation.

2.1 THE HARMONIC OSCILLATOR

A classical problem in mechanics is describing the motion of a mass on a spring. Once put into motion, the mass starts moving there and back again. This repeated motion is called an oscillation. The oscillations occur because the spring exerts a restoring force, pulling the mass back to arrive at its starting position after a period of time. The force acting on the mass m depends on the displacement from equilibrium z and the spring constant k of the spring, a law first described by Robert Hooke.[23] By applying Newton's laws of motion,[24] one can write:

$$\Sigma F_{mass} = m\frac{d^2z}{dt^2} + kz$$

Since solutions to the trajectory of the mass can be described by sinusoids, the oscillator is called harmonic. In reality the amplitude of the motion will slowly decay. Damping causes energy loss from the system. Damping forces depend on the velocity of the mass $\frac{dz}{dt}$ and the damping constant c:

$$\Sigma F_{mass} = m\frac{d^2z}{dt^2} + c\frac{dz}{dt} + kz$$

In order to overcome the energy losses caused by damping one can drive the system by an external force. When the mass on the spring almost stops, one can pull it again to continue the movement. The addition of the external driving force F_{ext} makes us arrive at the final expression for the displacement of the mass on a spring:

$$F_{ext}(t) = m\frac{d^2z}{dt^2} + c\frac{dz}{dt} + kz \tag{2.1}$$

The importance of this equation cannot be stressed enough. It does not only describe the motion of a simple mass on a spring, but extends to various mechanical systems (speakers, car suspensions, clocks) as well as electrical (filters, amplifiers) and quantum systems.[25,26] In this thesis it is used to describe the movement of the center of the graphene membrane.

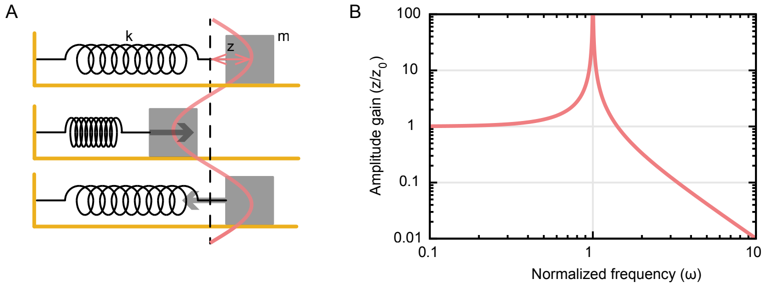

Figure 2.1: A) Motion of a mass on a spring as described by eq. 2.1, performing a harmonic oscillation. B) Frequency response of a harmonic oscillator around its resonance frequency.

2.2 SINUSOIDALLY DRIVEN OSCILLATOR

In the experiments performed for this thesis the membranes are driven by a sinusoidal drive. To investigate the behavior of a sinusoidally driven oscillator we rearrange eq. 2.1 with different constants: $\omega_0 = \sqrt{k/m}$ and $\zeta = \frac{c}{2\sqrt{mk}}$. The meaning of these constants will become clear shortly. Together with the replacement of the external drive term with a sinusoidal force $F_0 \sin(\omega t)$ this gives the following expression:

$$\frac{d^2 z}{dt^2} + 2\zeta\omega_0 \frac{dz}{dt} + \omega_0^2 z = \frac{F_0}{m}\sin(\omega t) \tag{2.2}$$

Solutions to this equation for the displacement z are sinusoidal oscillations at the same frequency as the driving force. A typical response of a driven harmonic oscillator is shown in figure 2.1. The amplitude gain of the solution relative to the driving amplitude varies with driving frequency ω, as shown in panel B. At driving frequency $\omega = \omega_0$ a resonance peak appears in the frequency response. This special frequency is called the resonant frequency. The graphed behavior can be understood as follows.

- $\omega << \omega_0$: The drive oscillates very slow. The inertia of the mass is small as compared to the stiffness of the spring and the displacement z simply follows the applied drive. Therefore, the amplitude gain is 1.
- $\omega = \omega_0$: The drive oscillates at exactly the right frequency to add energy to the system. This is comparable to pushing a swing to make someone get higher. The force is in phase with the velocity and the amplitude gain reaches a peak value.
- $\omega >> \omega_0$: The drive oscillates very fast. The inertia of the mass is too big as compared to the stiffness of the spring and movement cannot keep up with the drive. The force is in antiphase with respect to the velocity and the gain diminishes; the mass is almost at rest.

The parameter ζ sets the width of the resonance peak. This parameter is called the damping term. With low damping, the peak is very high and narrow. With high damping instead, the peak lowers and broadens. The sharpness of the peak is expressed in the full bandwidth at half maximum (FBHM) of the magnitude $\Delta\omega = \omega_{\text{right,HM}} - \omega_{\text{left,HM}}$. The Q - factor is a related parameter, defined as the ratio of the bandwidth of the resonance peak over the center frequency. It can be expressed in the damping term ζ:

$$Q \equiv \frac{\omega_0}{\Delta\omega} = \frac{1}{2\zeta} \tag{2.3}$$

2.3 DAMPING

Several mechanisms can cause energy dissipation in an oscillating microsystem. An obvious damping mechanism is gas friction, which can be minimized by operating in high vacuum conditions. Two specific mechanisms are discussed more in depth: thermoelastic Zener damping and Akhiezer damping.

2.3.1 Thermoelastic damping

First described by Zener in 1937, thermoelastic damping is an internal dissipation mechanism arising from heat gradients in the material.[27] The original theory considers that elastic strains in the material cause heating. The induced heat flow consumes energy from the oscillating system. For an infinitely thin material the internal damping can be written as:

$$Q^{-1} = \frac{\alpha^2 T E}{c_p} \frac{\omega \tau_{th}}{1 + \omega^2 \tau_{th}^2} \tag{2.4}$$

where c_p is the specific heat, T is temperature, α is the thermal expansion coefficient, E the Young's modulus and τ_{th} a thermal constant describing the speed of temperature equilibration.[28] This equation reaches a peak value at $\omega\tau_{th} = 1$, indicating that damping is highest close to a specific frequency.

2.3.2 Akhiezer damping

The scattering of phonon modes among each other can be a source of internal damping, as first described by Bommel et al.[29] Approximating to scattering between two bands in bulk, the Akhiezer damping can be written as:

$$Q^{-1} = \frac{c_p T \lambda_{av}^2}{\rho v^2} \frac{\omega \tau_{ph-ph}}{1 + \omega^2 \tau_{ph-ph}^2} \tag{2.5}$$

where c_p is the specific heat, T is temperature, λ_{av}^2 is the Grüneisen parameter, ρ the material density and τ_{ph-ph} a constant describing the intensity of phonon interactions. However, simulations suggest that this is not the right expression for a two dimensional material.[30] It is rather correct to solve the Boltzmann transport equation to find exact values, for which the following relation holds:

$$Q^{-1} \propto \omega \tag{2.6}$$

This kind of behavior has been recently reported for carbon nanotubes.[31] It is therefore likely to be applicable for the case of graphene membranes.

2.4 PHASE

To fully describe a sinusoidal motion with given frequency, one needs to know both its amplitude and phase. Phase describes a relative point in time. The phase can be relative to a zero crossing as well as to another signal. Professional dancers are generally a good example of two motions that are in phase. Beginning dancers are often out of phase - both in respect to the music as well as their partner - with all consequences. The sinusoidal motion of the membrane and the driving force can be shifted in phase with respect to

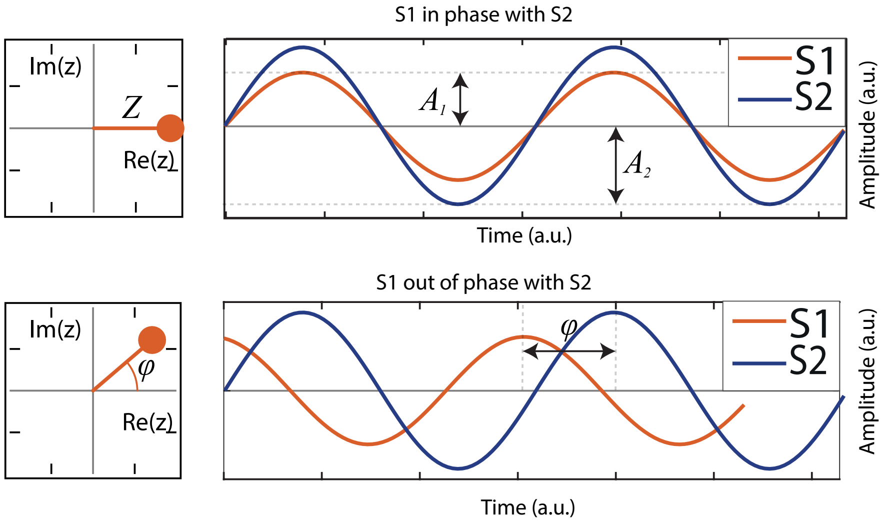
S1 in phase with S2

S1 out of phase with S2

Figure 2.2: The relation between two signals S1 and S2 is represented in the complex plane by a phase angle ϕ and an amplitude $Z = \frac{A_2}{A_1}$.

each other. Using Euler's formula one can write for two sinusoidal signals with amplitudes A_1 and A_2:

$$A_1 e^{i\omega t} = A_2 e^{i\omega t + \phi} \tag{2.7}$$

The relation between the signals is represented in the complex plane by a phase angle ϕ and a magnitude $Z = \frac{A_2}{A_1}$. Figure 2.2 shows two sets of signals. One set is in phase and the other set is out of phase. Projections onto the real and imaginary axis are shown, representing the component in phase and out of phase. In the experiments, the membranes motion with respect to the driving force is measured, which in essence is a measurement of the transfer function of the system. The representation with a real and an imaginary part will be used throughout the thesis to distinguish the component of the membrane motion that is in phase with respect to the drive from the component that is out of phase with respect to the drive.

2.5 IMPACT OF DEFECTS

The harmonic oscillator describes the motion of the center of the membrane with two key parameters: its resonance frequency ω_0 and its Q-factor. The presence of pores alters these parameters by changing several characteristics. The effect of defects caused by ion bombardment on the membrane mechanics are not obvious. The perforations can be seen as changes in either the macroscopic values of the Young's modulus, material density and in plane stress or changes on the atomistic scale in chemistry and grain boundaries. Each of these is discussed separately. For graphene nanodrums, it can be stated as a general rule that structural defects decrease the resonant frequency and chemical defects increase the resonant frequency. This has been confirmed by Robinson et al. for argon irradiated graphene.

2.5.1 Young's modulus

Theoretical studies suggest that the Young's modulus of graphene will decrease with increasing porosity p by a value of 24GPa per cent porosity fraction.[33] Porosity is defined as the ratio between the total permeation area A_{pore} and the area of the nanodrum A_{drum}:

$$p = A_{\text{pore}} / A_{\text{drum}} \tag{2.8}$$

Assuming that the the Young's modulus is proportional to the stiffness of the oscillator, $E \propto k$, both the resonance frequency and the Q-factor should decrease with increasing porosity. Based on porosities found in chapter 4, changes in the Young's modulus could attribute to a decrease in frequency and Q factor of up to 5%.

2.5.2 Density

Variation in the membrane density, which is proportional to $1 - p$, changes the characteristics of the mechanical resonance to a negligible extent of less than 1%. Oxidation of the graphene might affect this value.

2.5.3 Stress

The membranes have a pretension induced by the process of transfer. MD simulations suggest a decrease in the pretension after perforation, attributable to a decrease in the Young's modulus.[34] A lower pretension would decrease the mechanical resonance frequency and Q factor accordingly.[35]

2.5.4 Grain boundaries

Several publications found counter intuitive results using MD simulations, indicating that grain boundary defects can strengthen the graphene.[36] Wei et al. concludes that grain boundary defects can either increase or decrease the Young's modulus of graphene, and the mechanism relies on the detailed arrangement of the defects, and not just their density. On the other hand, indentation tests on CVD graphene show that heat induced oxidation of the boundaries weakens the material, but the effect on the Young's modulus is not addressed.[38] In summary, the impact of changes to the graphene surface and grain boundaries on the mechanical properties of graphene is not yet fully understood.

2.6 GAS FLOW

Nanopores facilitate gas permeation through the membrane. The permeation speed depends on the pore size and the type of gas. A core parameter for the physics of gas permeation through perforated membranes is the Knudsen number.[39] It relates the mean free path of gas molecules λ to the characteristic dimension d_p of the aperture:

$$\text{Kn} = \frac{\lambda}{d_p} \tag{2.9}$$

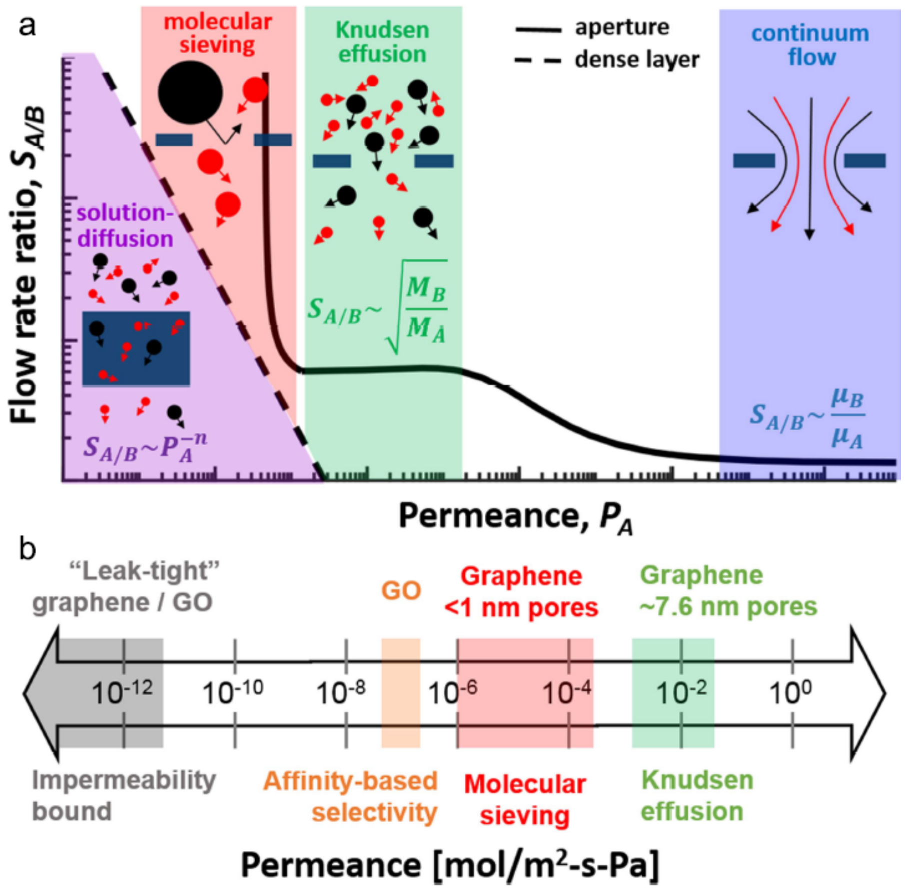
a
molecular sieving
Knudsen effusion
aperture
dense layer
continuum flow
Flow rate ratio, $S_{A/B}$
solution-diffusion
$S_{A/B} \sim \sqrt{\frac{M_B}{M_A}}$
$S_{A/B} \sim P_A^{-n}$
$S_{A/B} \sim \frac{\mu_B}{\mu_A}$
Permeance, P_A
b
"Leak-tight" graphene / GO
GO
Graphene <1 nm pores
Graphene ~7.6 nm pores
10^{-12}
10^{-10}
10^{-8}
10^{-6}
10^{-4}
10^{-2}
10^{0}
Impermeability bound
Affinity-based selectivity
Molecular sieving
Knudsen effusion
Permeance [mol/m^2-s-Pa]

Figure 2.3: A) Selectivity of gas particles with different size as compared to the pore size in a membrane. A trade-off exists between permeance and selectivity B) Typical permeability regimes. Figure reproduced from Boutilier et al.

Permeation is dominated by a certain mechanism according to the value of the Knudsen number.[40,41] As depicted in Figure 2.3, three regimes can be identified for porous materials.

- $\mathrm{Kn} \ll 1$: Continuum flow
- $\mathrm{Kn} > 1$: Knudsen effusion
- $d_{\text{aperture}} \approx d_{\text{molecule}}$: Molecular sieving

For large perforations, when $\mathrm{Kn} \ll 1$, continuum physics describe the flow through the pores. In the Knudsen effusion regime, it is statistical physics that describes the particle interactions. For even smaller pores, the interactions of single atoms need to be studied. The solution-diffusion area applies to dense (non-porous) materials, in which gasses dissolve and diffuse.

2.6.1 Continuum flow

When perforations are large, and $\mathrm{Kn} \ll 1$, the gas flow is described by the viscosity μ of the flowing medium and the geometry of the perforation. For the viscosity, the particle interactions among each other are more important than interactions with the surrounding. Therefore, the viscosity is gas specific. For an infinitely thin geometry Sampson's model describes the flux Φ through an orifice of diameter d_p.[42]

$$\Phi = \frac{\Delta P d_p^3}{24\mu} \tag{2.10}$$

The ratio between gas viscosities $\frac{\mu_B}{\mu_A}$ determines the selectivity for a mixture of gasses. In the continuum flow regime a high permeance can be achieved at the exchange of low selectivity.

2.6.2 Classical effusion

In the Knudsen regime, where $\mathrm{Kn} > 1$, the average distance between gas particles is higher than the size of the aperture. The outflow of gas is therefore governed by the incident rate of free gas particles on the aperture area. Generalized to a flux Φ the equation sounds:

$$d\Phi(v) = n v_z f(\vec{v}) d^3\vec{v}$$

Where n is the number of particles, $f(\vec{v})$ is the three dimensional particle speed distribution and v_z is the speed component perpendicular to the aperture area $|v|\cos(\theta)$.[43] For an ideal gas with N particles having a Maxwellian speed distribution $< v >=\sqrt{\frac{8K_BT}{\pi m}}$, the flux Φ can be expressed in the mass m of the gas particles, and the ensemble pressure P and temperature T:

$$\Phi = N\sqrt{\frac{K_BT}{2\pi m}} = \frac{P}{\sqrt{2\pi m K_B T}} \tag{2.11}$$

The escape rate of particles from a closed cavity with volume V depends on the aperture area A and the escape probability γ. Solving the following differential equation leads to a time constant τ characterizing the gas – aperture interaction:

$$\frac{dn}{dt} = \frac{\Delta P A \gamma}{\sqrt{2\pi MRT}}$$

$$n = n_0 e^{\frac{A\gamma}{V}\sqrt{\frac{RT}{2\pi M}}t} = n_0 e^{t/\tau}$$

In the Knudsen regime the time constant τ_{eff} characterizing gas effusion through pores of cumulative area A is given by:

$$\tau_{eff} = \frac{V}{A\gamma}\sqrt{\frac{2\pi M}{RT}} \tag{2.12}$$

where V is the volume of the cavity from which the gas escapes, M is the molar mass of the gas and RT the thermal energy. The ratio between the molar masses $\frac{M_B}{M_A}$ determines the selectivity for a mixture of gasses.

2.6.3 Molecular sieving

In the molecular sieving regime the aperture size is similar to the molecule size and Van der Waals forces constitute to a potential bump that has to be overcome by the sieved particles. For pores bigger than the molecule size this interaction can be modelled by introducing an effective aperture area A_{effect} which depends on the pore and molecule diameters d_p and d_m:

$$A_{\text{effect}} = \pi/4(d_p - d_m)^2 \tag{2.13}$$

Whenever to molecule dimensions are comparable or bigger than the aperture dimensions a more elaborate model has to be thought of. Arrhenius' concept of activation energy can be used to picture that the aperture is a potential bump that can be overcome by thermal energy fluctuations.[44] Using the error function we arrive at an expression for the escape probability γ:

$$\gamma = 1/2\text{erfc}\left(\sqrt{\frac{E_a}{K_B T}}\right) \tag{2.14}$$

The potential barrier E_a can be modeled as a Leonard-Jones potential.[45] For precise solutions which include effects of adsorption and surface diffusion, molecular dynamics modeling is required. An approximation can be given in terms of the gas-carbon interaction parameters ϵ and σ and the graphene bond length $a = 0.154$ nm:

$$E_a \approx \frac{\pi d_p}{a} 4\epsilon \left(\left(\frac{\sigma}{d_p/2} \right)^{12} - \left(\frac{\sigma}{d_p/2} \right)^{6} \right) \tag{2.15}$$

Molecular sieving can achieve highest selectivities at the cost of low flow rates. Achieving consistent performance is hard, since pores need to be extremely small and have a narrow size distribution.

3 METHODS

The samples discussed in this thesis consist of a perforated graphene layer covering circular cavities. The devices are measured optically, using lasers to actuate the graphene membranes and at the same time read out the deflection. The experiments consist of varying pressure and gas while measuring the changes in mechanical response of the moving membranes. This chapter first discusses the interferometric setup used throughout the experiments. Afterwards, it goes in depth on the actuation through modulated absorption and read-out by interferometry.

3.1 INTERFEROMETRY SETUP

The frequency response curves of the samples are measured with an interferometry setup. The measurement setup shown in figure 3.1 consists of two lasers aimed at the Fabry-Perot cavity in a pressure chamber. The red laser is used for interferometry with the membrane acting as a moving mirror and the bottom of the cavity as rigid mirror, whereas the modulated blue laser actuates the membrane.[17] The beams are focused on the sample with a 1.5 μm spot size. The red and blue laser power are 2 mW and 0.3 mW respectively. A network calibration measurement is performed, which involves directly aiming the blue laser at the photodiode, to eliminate systematic parasitic delays due to imperfections in equipment and wiring.

3.2 ACTUATION

One layer of graphene absorbs around 2.7% of the incoming light.[46] Absorption of light causes heating of the graphene. Blue laser absorption is two times higher than that of the red laser, since its wavelength is closer to the absorption peak in the ultraviolet region at 270 nm. Therefore, the blue laser (λ = 405 nm) is used to actuate the membrane. The laser intensity is modulated, causing periodic variation of the membrane tension by thermal expansion.[47] The periodic stretching and shrinking of the membrane sets it in motion. This way of actuation will be referred to as optothermal actuation.

3.3 READ-OUT

The deflection of the graphene membrane is measured by interferometric read-out using a red laser (λ = 632.8 nm). The fraction of the light reflected directly from the membrane interferes with the fraction reflected from the silicon substrate. When the two signals are in phase, they interfere construc-

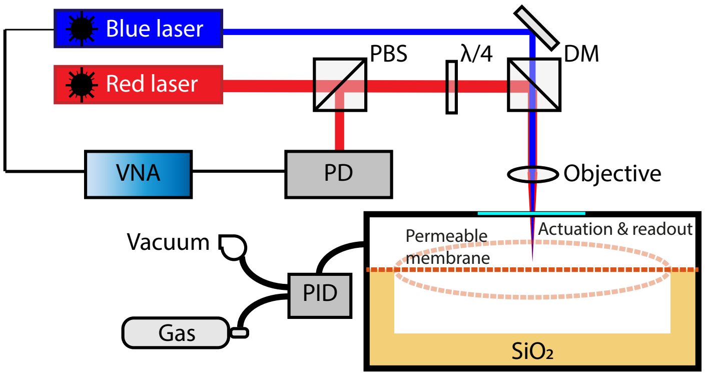

Figure 3.1: Interferometry setup used to perform the experiments. The red laser passes subsequently through the polarized beam splitter (PBS) and the quarter-wave plate ($\lambda/4$), after which it is combined with the blue laser using a dichroic mirror (DM) and focused on the nanodrum. The readout is performed by a high frequency photodiode (PD) which output is fed into the Vector Network Analyzer (VNA). The VNA modulates the blue laser which actuates the membrane. Gas pressure inside the vacuum chamber is controlled by a PID controller.

tively and a high reflectivity is measured. Instead, when the signals are out of phase, the apparent reflectivity is low. Small changes in the distance between the two mirrors in the order of nanometers cause big changes in the apparent reflectivity.

A polarized beam splitter and a quarter-wave plate are used to separate the reflected light from the incident laser light. The polarized beam splitter is transparent for one polarization and reflects light with a perpendicular polarization. The reflected light passes the quarter-wave plate twice, effectively changing polarization in such way that the light that passed on its way towards the membrane will reflect on its way back and shine into the photodiode. A diagram of the setup is shown in 3.1. In the figure the path of the light rays can be tracked from the laser onto the sample and back into the photodiode.

4 CHARACTERIZATION

Experiments are performed on devices accommodating the measurement of gas permeation trough porous graphene membranes on a silicon chip. The devices consist of a perforated graphene layer covering circular cavities. The nanodrums are made on a silicon substrate patterned with circular wells of 300 nm depth and diameters of 1, 2 and 3 μm using Reactive Ion Etching. A single layer of CVD graphene is transferred on top of the wells. The graphene has been exposed to highly energetic ion bombardment with $129Xe^{23+}0.71MeV/u$, with a flux ranging from $5.09 \cdot 10^7$ to $5.09 \cdot 10^9$ ions per square centimeter at the SME beamline of GANIL (Caen, France). This is similar to the treatment described by Madauß et al. Also, unperforated devices are available for reference. The defects induced to the graphene layer have been characterized by atomic force microscopy (AFM). An unperforated sample is discussed first. Then, two samples that are shown in the gas permeation results chapter are discussed more in depth. The gas permeation samples have been bombarded with a flux of $5.09 \cdot 10^9$ ions per square centimeter, unless stated otherwise. This agrees with around 360 pores on a 3 μm drum.

4.1 AN UNPERFORATED NANODRUM

Figure 4.1 shows an AFM scan of an unperforated nanodrum with a diameter of 3 μm. The graphene is clearly wrinkled and a prominent vertical crease is visible. This kind of imperfections, caused by straining during transfer or thermal fluctuations, are expected to occur and are discussed in depth by Deng and Berry. Since no holes or other defects are visible, this membrane is a good example of a pristine drum which is expected to be fairly impermeable. The membrane is noticeably lower at the borders of the drum, which might indicate slight wall adhesion.

4.2 GAS PERMEATION SAMPLE 1

The AFM measurements in figure 4.2 show a height scan of sample 1. The enlarged area in B proves that ion bombardment has created nanopores with an average size of 14 nm. The pores are most pronounced in the inset, where they are visible as black dots surrounded by a white area. The white areas might consist of graphene oxide that has grown after the pores have been exposed to the laser.[49] The white areas do not show up on samples before laser measurements. Moreover, they are most pronounced in the center of the membrane where the laser spot was focused. The pores are distributed evenly, which is best seen outside of the membrane area. Tiny, white spots mark the defective areas in the graphene. The picture resolution is not sufficient to distinguish the indentations them selfs in this area.

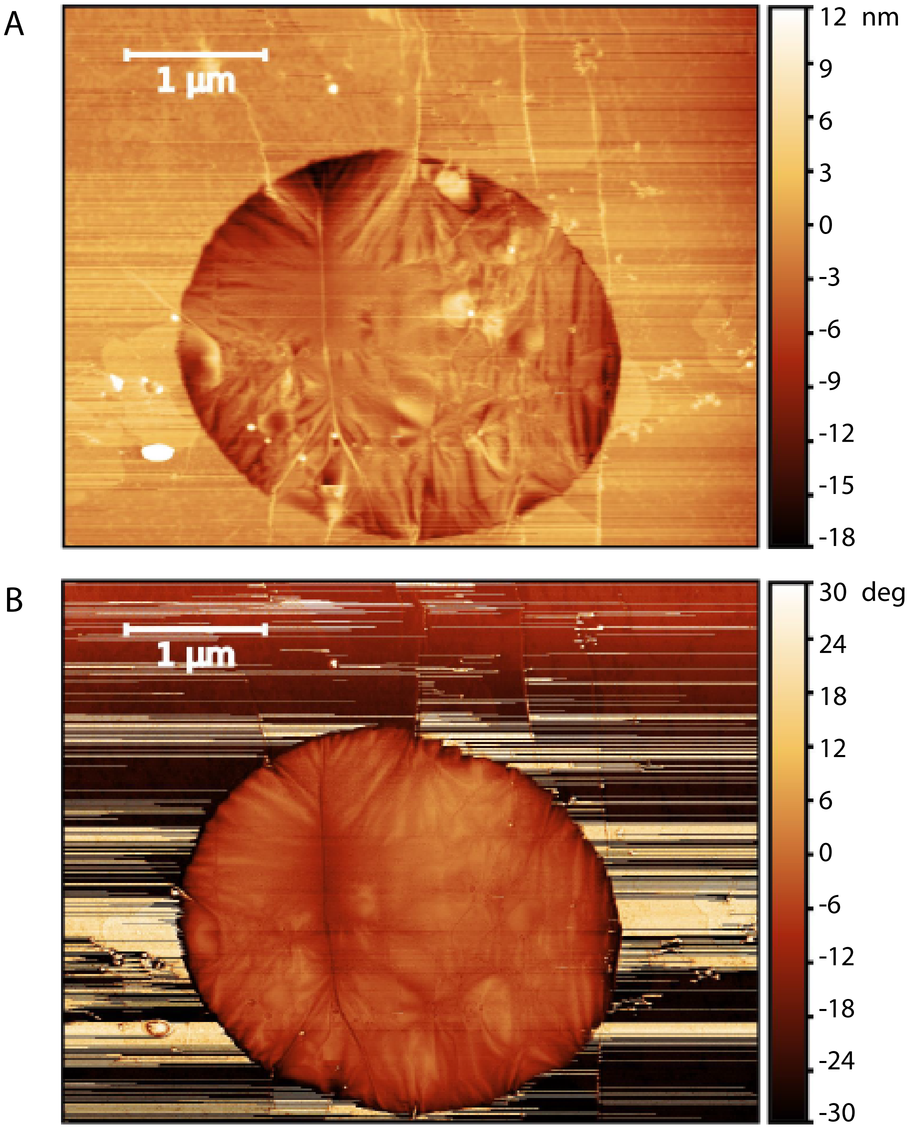
A
1 µm
12 nm
9
6
3
0
-3
-6
-9
-12
-15
-18
B
1 µm
30 deg
24
18
12
6
0
-6
-12
-18
-24
-30

Figure 4.1: Characterization of an unperforated 3 μm drum using AFM. Both the height channel (A) and the phase channel (B) are shown. The scans show that the graphene is wrinkled but not perforated.

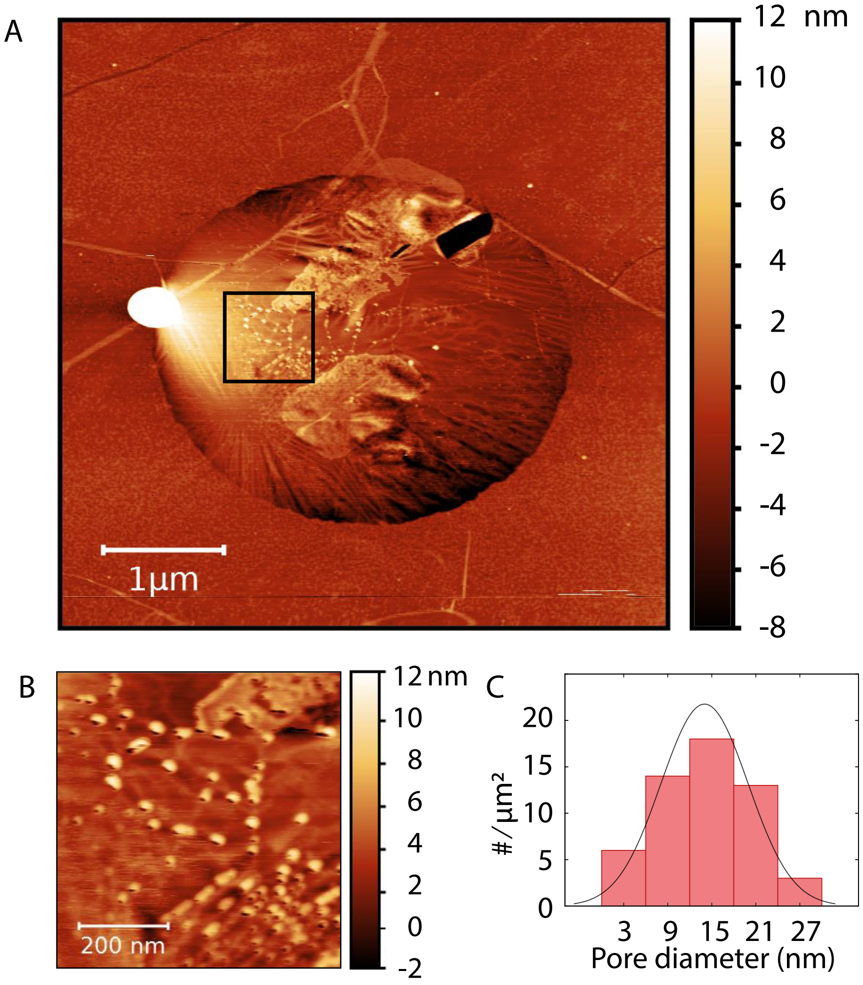

Figure 4.2: Characterization of the indentations on sample 1 using AFM. A) Full height scan of the drum with an inset square indicating the enlarged area. B) Nano pores are visible as small, black dots surrounded by a white area. (C) Nano pore size distribution with mean 14 nm and a standard deviation 6 nm based on statistics on 54 pores.

The scans show that the membrane is ruptured on a square area of 470 by 120 nm in the top right part. This big hole accounts for 52% of the total effusion area of 0.1 μm². The large, white circle on the left is probably a water droplet.

4.3 GAS PERMEATION SAMPLE 2

The AFM measurements in figure 4.3 show a height scan of sample 2. The enlarged area in B again proves that ion bombardment has created nanopores, here with an average size of 10 nm. The pores are most pronounced in the inset, where they show up as black dots surrounded by a white area. The white areas might consist of graphene oxide that has grown after the pores have been exposed to the laser.[49] The white areas do not show up on samples before laser measurements. Moreover, they are most pronounced in the center of the membrane where the laser spot was focused. The pores seem

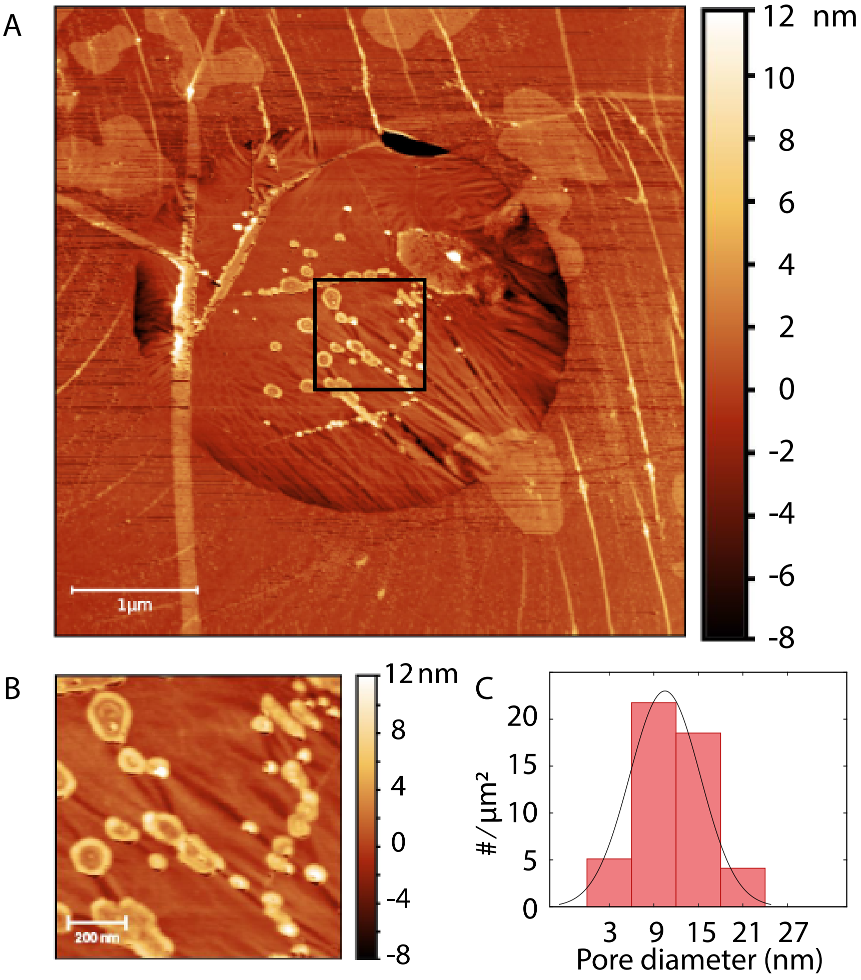

Figure 4.3: Characterization of the indentations on sample 2 using AFM. A) Full height scan of the drum is shown in A with an inset squares indicating the enlarged area. B) Nano pores are visible as small, black dots surrounded by a white area. (C) Nano pore sizes are distributed normally with mean 10 nm and standard deviation 5 nm based on statistics on 51 pores.

to have induced several cracks in the graphene. On the left side of the drum a vertical fold is visible in the graphene, consisting of stacked graphene layers.[50] The scans show that the membrane is ruptured on an area of 450 by 125 nm in the top right part. This big hole accounts for 66% of the total effusion area of 0.15 μm^2.

4.4 MECHANICAL CHARACTERIZATION

The mechanical response of both perforated and unperforated samples has been measured in vacuum. The changes in mechanical properties of the graphene caused by the bombardment are studied by performing measurements of the frequency and the Q-factor of the first mechanical resonance.

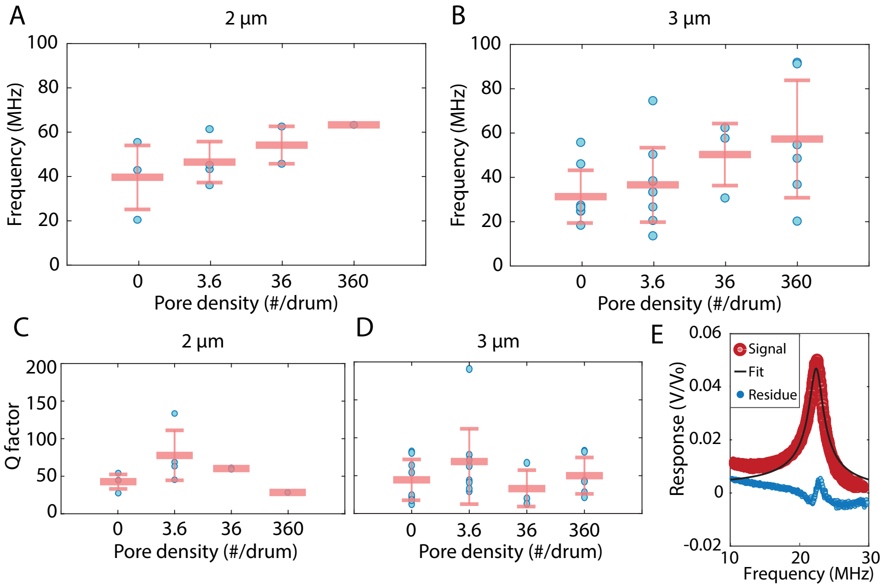

Figure 4.4: Frequency (A & B) and Q-factor (C & D) of the first mechanical resonance for varying pore density. The mean and standard deviation is indicated by red marks. Results of 2 and 3 μm drums are presented separately. The measurements hint a trend of increasing frequency with higher pore density, but the error margins are large. Values are obtained by fitting a Lorentzian to the response (E).

In figure 4.4 panel A to D display the relation between the fluence and the resonant frequency and the Q-factor for 2 and 3 μm drums. These values are obtained by fitting a Lorentzian shape to the measured frequency response as shown in panel E. Naturally, the small drums show higher mechanical resonance frequency and Q factor. The effect of defects caused by ion bombardment is less obvious. The measurements of the frequency of the first mechanical resonance suggest a correlation with the porosity, but the error margins caused by inter device variations are too big to make definitive conclusions. Assuming that the visible trend is indeed true, this kind of behavior would indicate that chemical defects play a dominant role in the tension of the membrane.

5 GAS PERMEATION MODEL

This chapter presents the model describing the response of a perforated graphene membrane in the presence of gas. First, the important aspects of the model are summarized. The following sections go in depth into the exact derivation of the model. The differential equations are compared to an equivalent electric circuit, which is simulated using Simulink.

5.1 MODEL SUMMARY

The motion of the membrane responds both to the optothermal actuation by a modulated blue laser and the pressure build-up inside the cavity. The optothermal response in vacuum is used by Dolleman et al. to characterize the heat transport from a membrane to the substrate. The temperature of the membrane T is shown to follow a first order differential equation depending on the thermal flux delivered by the laser $\frac{\mathcal{P}_{AC}}{C_T}e^{i\omega t}$ and the thermal equilibration time constant τ_{th} for heat escaping the system:

$$\frac{d\Delta T}{dt} + \frac{\Delta T}{\tau_{th}} = \frac{\mathcal{P}_{AC}}{C_T}e^{i\omega t} \tag{5.1}$$

Here C_T is the effective thermal capacity of the system. In the presence of gas, this model has to be extended. We consider two mechanisms that can change the pressure inside the cavity: gas expansion upon heating of the gas and gas compression by the movement of the membrane.

The pressure inside the cavity changes isometrically as a result of direct laser heating $\frac{\mathcal{P}_{AC}}{C_{gas}}e^{i\omega t}$ and isothermally by compression from the movement of the membrane $\gamma dz/dt$, where z is the membrane deflection. Energy flows through the walls of the cavity are neglected. The permeation resistance R_{gas} governs the gas flow driven by the pressure difference between the cavity and the outside. The RC model with gas permeation time constant $\tau_{gas} = R_{gas}C_{gas}$ for the pressure inside the cavity can now be written:

$$\frac{d\Delta P}{dt} + \frac{\Delta P}{\tau_{gas}} = \frac{\mathcal{P}_{AC}}{C_{gas}}e^{i\omega t} + \gamma\frac{dz}{dt} \tag{5.2}$$

Here C_{gas} is the effective gas capacity of the system. The contributions of both the thermal drive and the pressure inside the cavity need to be added to obtain the driving force causing the membrane to deflect. The one dimensional harmonic oscillator describes the motion of the center of the membrane:

$$m\frac{d^2z}{dt^2} + c\frac{dz}{dt} + kz = \alpha\Delta T + \beta\Delta P \tag{5.3}$$

Here α is an effective thermal expansion coefficient and β is the linear pressure-deflection relation which has been derived in chapter 5.3. The resulting complex expression for a sinusoidal drive representing the frequency

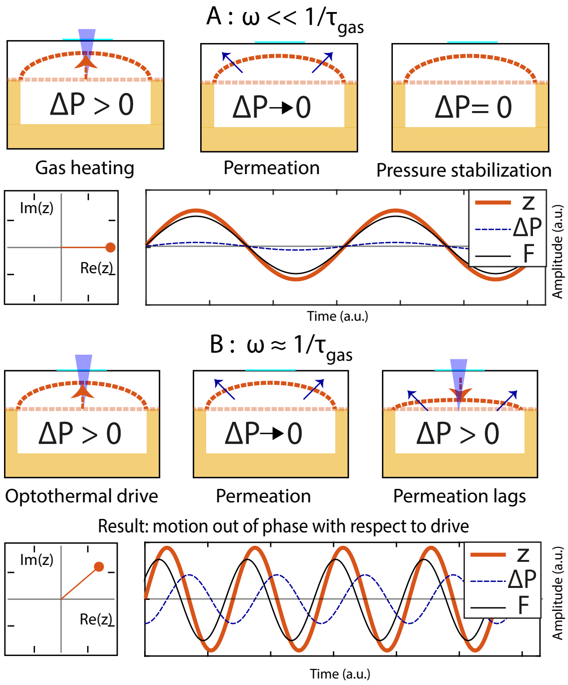
A : ω << 1/τgas
ΔP > 0
ΔP→0
ΔP= 0
Gas heating
Permeation
Pressure stabilization
Im(z)
Re(z)
z
ΔP
F
Amplitude (a.u.)
Time (a.u.)
B : ω ≈ 1/τgas
ΔP > 0
ΔP→0
ΔP > 0
Optothermal drive
Permeation
Permeation lags
Result: motion out of phase with respect to drive
Im(z)
Re(z)
z
ΔP
F
Amplitude (a.u.)
Time (a.u.)

Figure 5.1: Schematic of the membrane deflection and the pressure inside the cavity as a response to the optothermal drive. At low frequencies the gas has sufficient time to permeate. At a frequency $\omega_{gas} = 1/\tau_{gas}$ the phase difference between the drive and the motion of the membrane is maximal.

response of the membrane below the resonance frequency is fully derived in the following chapters. The imaginary part of this expression is used to fit the experimental results with a, b, τ_{th} and τ_{gas} as free variables:

$$Im(z_\omega) = a\frac{\omega\tau_{th}}{1+\omega^2\tau_{th}^2} + b\frac{\omega\tau_{gas}}{1+\omega^2\tau_{gas}^2} + ab\frac{\gamma\omega\tau_{gas}(1-\omega^2\tau_{th}\tau_{gas})}{(1-\omega^2\tau_{th}\tau_{gas})^2+(\omega\tau_{th}+\omega\tau_{gas})^2} \tag{5.4}$$

At frequencies close to the reciprocal permeation time $\omega_{gas} = 1/\tau_{gas}$ the contribution of ΔP will cause motion out of phase with respect to the drive, as visualized in figure 5.1. The imaginary part of the response will reach a peak value at this characteristic frequency.

5.2 GAS PRESSURE INSIDE CAVITY

This section shows a derivation of the RC model for gas effusion. It is assumed that the gas trapped inside the cavity acts as a 'pressure reservoir' from which gas is escaping with a characteristic time constant. Remembering the results for the gas effusion time constant $\tau_{eff} = \frac{V}{A}\sqrt{\frac{2\pi M}{N_A K_B T}}$, one can write: $R = \frac{\sqrt{2\pi M N_A K_B T}}{A\gamma}$ and $C = \frac{V}{N_A K_B T}$. Here, C is the 'pressure capacity' of the system with pressure RC product $\tau_{eff} = RC$. It represents the excess amount of pressure inside the cavity. The gas resistance R_{gas} governing the RC product comes from the flow rate equation, which sounds:

$$\Phi_{gas} = \frac{P_{cav} - P_{sur}}{R_{gas}} \tag{5.5}$$

Gas flow is governed by the pressure difference between the cavity and the outside and the effusion resistance R. To describe the interaction with the moving membrane system we need to know the pressure increase when the gas is heated by the laser. With given gas specific heat capacity c_p we can find the expression for the pressure capacity and call it C_{gas}:

$$C_{gas} = nMc_p(\frac{\partial P}{\partial T})^{-1}_{V,n} = \frac{VMc_P}{N_A K_B} \tag{5.6}$$

Next, we derive a relation between the membranes compression $\frac{dz}{dt}$ and the pressure change $\frac{d\Delta P}{dt}$. For an infinitesimal part of the membrane we apply Boyle's law, which states that pressure and volume are inversely proportional. Approximating the trapped layer of gas as a squeezed film, one may write:

$$P_0 z_0 = P_1(z_0 + \delta z) \tag{5.7}$$

Substitution of $\Delta P = P_0 - P_1$ leads to:

$$P_0 \delta z = \Delta P(z_0 + \delta z) \tag{5.8}$$

Now, as long as $\Delta P \ll P_0$ and $\delta z \ll z_0$ we get the following expression:

$$\Delta P = \frac{P_0}{z_0}\delta z = \gamma \delta z \tag{5.9}$$

The RC model with permeation time constant $\tau_{gas} = R_{gas}C_{gas}$ for the pressure inside the cavity can now be written:

$$\frac{d\Delta P}{dt} + \frac{\Delta P}{\tau_{gas}} = \frac{\mathcal{P}_{AC}}{C_{gas}} e^{i\omega t} + \gamma \frac{dz}{dt} \tag{5.10}$$

This is the same as equation 5.2 in chapter 5.1.

5.3 PRESSURE – DEFLECTION RELATION

A pressure difference ΔP between the two sides of the membrane bulges the membrane up, constituting to an increased tension in the membrane. As the force applied by the pressure is evenly distributed over the membrane, the membrane will attain the shape of a truncated sphere with uniform curvature r. A force balance for a pressurized sphere with a thin wall of thickness t, relates the tensile stress σ in the walls of the sphere to the pressure:

$$\sigma 2\pi r t = \Delta P \pi r^2$$

$$\Delta P = \frac{2\sigma t}{r} \tag{5.11}$$

As long as the deflection in the center of the graphene membrane with radius a is small, it can be approximated using the formula:

$$\delta z \approx \frac{(2a)^2}{2r} \tag{5.12}$$

Therefore, for small deflections, one may write:

$$\beta = \frac{\delta z}{\Delta P} = \frac{a^2}{\sigma t} \tag{5.13}$$

The factor β relates the pressure difference to the deflection of the membrane and its tensile forces.

5.4 FULL MODEL DERIVATION

The equation of motion for the membrane sounds:

$$m\frac{d^2z}{dt^2} + c\frac{dz}{dt} + kz = \alpha\Delta T + \beta\Delta P \tag{5.14}$$

Here, α, β are respectively the linear thermal expansion coefficient and the linear coefficient from the pressure - deflection relation. For frequencies well below the resonance frequency the induced amplitude can be approximated by:

$$z_\omega e^{i\omega t} \approx \alpha\Delta T_\omega + \beta\Delta P_\omega \tag{5.15}$$

This can be inserted into equation 5.10 to arrive at an expression for ΔP_ω:

$$\frac{d\Delta P}{dt} + \frac{\Delta P}{(1-\beta\gamma)\tau_{gas}} = \frac{\gamma\alpha}{(1-\beta\gamma)}\frac{d\Delta T}{dt} + \frac{\mathcal{P}_{AC}}{C_{gas}}e^{i\omega t} \tag{5.16}$$

The expression still depends on the temperature ΔT of the membrane. A solution for ΔT following equation 5.1 is given by Dolleman et al.:

$$\Delta T_\omega = \frac{R_{th}\mathcal{P}_{AC}}{i\omega\tau_{th}+1}e^{i\omega t} \tag{5.17}$$

This solution is used to arrive at:

$$\frac{d\Delta P}{dt} + \frac{\Delta P}{(1-\beta\gamma)\tau_{gas}} = \frac{\gamma\alpha R_{th}\mathcal{P}_{AC}}{(1-\beta\gamma)}\frac{i\omega e^{i\omega t}}{i\omega\tau_{th}+1} + \frac{\mathcal{P}_{AC}}{C_{gas}}e^{i\omega t}$$

$$\Delta P_\omega = \gamma\alpha R_{th}\mathcal{P}_{AC}\tau_{gas}\frac{i\omega e^{i\omega t}}{i\omega\tau_{th}+1}\frac{1}{i\omega\tau_{gas}+1} + \frac{(1-\beta\gamma)R_{gas}\mathcal{P}_{AC}}{i\omega\tau_{gas}+1}e^{i\omega t}$$

$$\begin{aligned}\Delta P_\omega = \gamma\alpha R_{th}\mathcal{P}_{AC}\tau_{gas}&\frac{i\omega e^{i\omega t}}{-\omega^2\tau_{th}\tau_{gas}+i\omega\tau_{th}+i\omega\tau_{gas}+1}\\ &+\frac{(1-\beta\gamma)R_{gas}\mathcal{P}_{AC}}{i\omega\tau_{gas}+1}e^{i\omega t}\end{aligned} \tag{5.18}$$

By inserting expressions 5.17 and 5.18 into formula 5.15, the complex amplitude z_ω can be obtained:

$$\begin{aligned}z_\omega e^{i\omega t} = \frac{\alpha R_{th}\mathcal{P}_{AC}}{i\omega\tau_{th}+1}e^{i\omega t} &+ \frac{(1-\beta\gamma)\beta R_{gas}\mathcal{P}_{AC}}{i\omega\tau_{gas}+1}e^{i\omega t}\\ &+\frac{\alpha\beta\gamma R_{th}\mathcal{P}_{AC}\tau_{gas}\cdot i\omega e^{i\omega t}}{-\omega^2\tau_{th}\tau_{gas}+i\omega\tau_{th}+i\omega\tau_{gas}+1}\end{aligned} \tag{5.19}$$

The imaginary part of this expression is calculated and used for fitting:

$$
\begin{aligned}
\mathrm{Im}(z_\omega) = \frac{\alpha\omega\tau_{th}R_{th}\mathcal{P}_{AC}}{1+\omega^2\tau_{th}^2} &+ \frac{(1-\beta\gamma)\beta\omega\tau_{gas}R_{gas}\mathcal{P}_{AC}}{1+\omega^2\tau_{gas}^2} \\
&+ \frac{\alpha\beta\gamma\omega\tau_{gas}R_{th}\mathcal{P}_{AC}(1-\omega^2\tau_{th}\tau_{gas})}{(1-\omega^2\tau_{th}\tau_{gas})^2+(\omega\tau_{th}+\omega\tau_{gas})^2}
\end{aligned}
\tag{5.20}
$$

This is the same as equation 5.4 in chapter 5.1.

5.5 EQUIVALENT ELECTRIC MODEL

The mechanisms governing the motion of the porous membrane are analogous to the currents running in an electric circuit. The equivalent circuit consists of a thermal, a mechanical and a pneumatic domain. In the following sections the domains are discussed one by one, highlighting similarities with the differential equations derived in the previous sections. Finally, the circuitry is simulated using Simulink.

5.5.1 Thermal

The optothermal drive actuating the membrane is represented by an AC voltage source in the left bottom of figure 5.2. It controls the voltage controlled current source driving an RC circuit consisting of a capacitor C_{th} and a resistor R_{th} in parallel. This circuit resembles the thermal flux delivered to the graphene with corresponding heat capacity and thermal boundary resistance. The equation for the membrane temperature (eq. 5.1) is written next to the equation for the currents running through this circuit:

$$
\begin{aligned}
\frac{d\Delta T}{dt} + \frac{\Delta T}{\tau_{th}} &= \frac{\mathcal{P}_{AC}}{C_{th}}e^{i\omega t} \\
C_{th}\frac{dV_C}{dt} + \frac{V_C}{R_{th}} &= i_{th}
\end{aligned}
$$

Comparison shows that the voltage across the capacitor V_C can represent the temperature of the membrane T. Thermal expansion sets the membrane in motion. Therefore, this voltage controls the source driving the circuit in the mechanical domain.

5.5.2 Mechanical domain

The mechanical motion of the membrane is represented by a driven damped harmonic oscillator. The motion for the membrane translates to an RLC circuit in figure 5.2 with a resistor $R_m = c$, an inductor $L_m = m$ and a capacitor $C_m = 1/k$, driven by two voltage controlled voltage sources, $V_{th} = \alpha\Delta T$ and $V_{gas} = \beta\Delta P$. The equation of motion (5.14) is written next to the expression for the electric potential in this circuit:

$$
\begin{aligned}
m\frac{d^2z}{dt^2} + c\frac{dz}{dt} + kz &= \alpha\Delta T + \beta\Delta P \\
L_m\frac{d^2q}{dt^2} + R_m\frac{dq}{dt} + \frac{q}{C_m} &= V_{th} + V_{gas}
\end{aligned}
$$

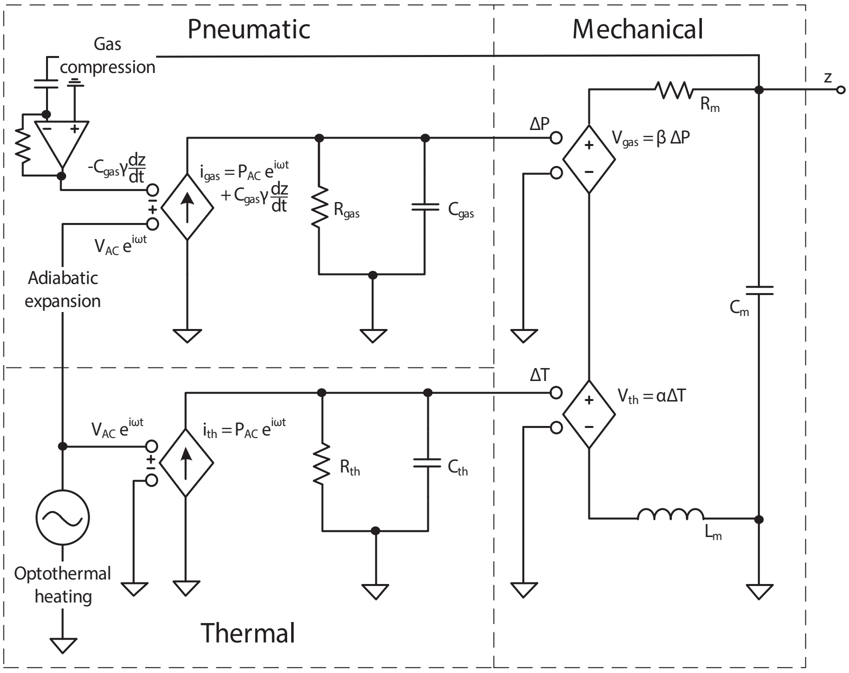
Pneumatic
Mechanical
Gas compression
-C_gas γ dz/dt
i_gas = P_AC e^iωt + C_gas γ dz/dt
R_gas
C_gas
ΔP
V_gas = β ΔP
R_m
z
V_AC e^iωt
Adiabatic expansion
C_m
ΔT
V_th = αΔT
V_AC e^iωt
i_th = P_AC e^iωt
R_th
C_th
L_m
Optothermal heating
Thermal

Figure 5.2: Equivalent electric model for the porous membrane.

Comparison shows that the charge q on the capacitor in this circuit can represent the deflection z of the membrane. In the schematic the voltage over the capacitor, $V_C = \frac{q}{C_m}$, is taken as an output for readout.

5.5.3 Pneumatic domain

The optothermal drive causing adiabatic expansion of the gas is represented by an AC voltage source in figure 5.2. Moreover, the movement of the membrane compresses the gas. The voltage over the capacitor in the mechanical domain kz controls a voltage controlled voltage source which is connected to a derivator to change the signal into the effective compression $-C_{gas}\gamma\frac{dz}{dt}$. A voltage controlled current source drives an RC circuit consisting of a capacitor C_{gas} and a resistor R_{gas} in parallel. This circuit resembles the pressure in the cavity with corresponding effective pressure capacity and permeation resistance. The equation for the pressure in the cavity (eq. 5.10) is written next to the equation for the currents running through this circuit:

$$\frac{d\Delta P}{dt} + \frac{\Delta P}{\tau_{gas}} = \frac{\mathcal{P}_{AC}}{C_{gas}} e^{i\omega t} + \gamma \frac{dz}{dt}$$

$$C_{gas}\frac{dV_C}{dt} + \frac{V_C}{R_{gas}} = i_{gas} + C_{gas}\gamma\frac{dz}{dt}$$

Comparison shows that the voltage across the capacitor V_C can represent the pressure inside the cavity P. The force exerted by the gas sets the membrane in motion. Therefore, this voltage controls the source driving the circuit in the mechanical domain.

Table 5.1: Details concerning the values used for the equivalent electric model.

	Symbol	Represented quantity	Value	Unit
Thermal	C_{th}	Heat capacity	$2.65 \cdot 10^{-15}$	F
	R_{th}	Thermal resistance	$1.32 \cdot 10^{7}$	Ω
Mechanical	L_m	Mass	$5.5 \cdot 10^{-15}$	H
	C_m	Stiffness	$3.7 \cdot 10^{-2}$	F
	R_m	Damping	$1.0 \cdot 10^{-8}$	Ω
Pneumatic	C_{gas}	Gas capacity	$8.53 \cdot 10^{-22}$	F
	R_{gas}	Permeation resistance	$9.43 \cdot 10^{14}$	Ω
	γ	Compression ratio	$2.0 \cdot 10^{10}$	

5.6 ELECTRIC MODEL SIMULATION

The equivalent electric model discussed in the previous chapter is used to simulate the results for gas permeation through the porous graphene membrane in Simulink. First, the numerical values used in the model are discussed. Then, the results from simulations are shown. The Simulink model together with the source code to run the simulation can be found on Github (url: `https://github.com/IrekRoslonStudent/thesis`).

5.6.1 Numerical values

The numerical values of the electrical components in figure 5.2 are to represent the physical reality. The components are discussed in the same order as they appeared in the previous sections. The numerical values used are collected in table 5.1.

THERMAL DOMAIN Based on the extensive discussion on the optothermal characterization by Dolleman et al., the heat capacity C_{th} of the suspended graphene as well as the thermal resistance R_{th} can be calculated using the formulas:

$$C_{th} = c_{p,g}\rho_g h_g \pi a^2 \tag{5.21}$$

$$R_{th} = (G_B h_g 2\pi a)^{-1} \tag{5.22}$$

Here $c_{p,g}$, ρ_g and h_g is are respectively the heat capacity, density and height of the graphene, and a is the membrane radius. The thermal resistance is attributed to limited boundary conductance G_B at the interface between the membrane and the supporting material, caused by phonon mismatch.[51] Based on thermal times measured in the next chapters the boundary conductance is set to 24 MW/m^{2}K to agree with a thermal equilibration time $\tau_{th} = 35$ ns, which is within the reported values of 30 ± 20 MW/m^{2}K.

MECHANICAL DOMAIN In the mechanical domain, the properties of graphene known from literature together with the expected resonance frequency ω_0 and Q-factor are used to model the RLC:

$$L_m = \rho_g h_g \pi a^2 \tag{5.23}$$

$$C_m = \frac{1}{\omega_0^2 L_m} \tag{5.24}$$

$$R_m = \frac{\omega_0 L}{Q} \tag{5.25}$$

The density of graphene is 0.77 mg/m^2.[2] Therefore one drum weighs $5.5 \cdot 10^{-15}$ kg. This is a minimum value, since contaminations on the drum are not taken into account.

PNEUMATIC DOMAIN The values for the gas capacity and permeation resistance are taken from effusion theory:

$$C_{gas} = \frac{V}{N_A K_B T} \tag{5.26}$$

$$R_{gas} = \frac{\sqrt{2\pi M N_A K_B T}}{A} \tag{5.27}$$

The gas compression ratio γ is calculated using:

$$\gamma = \frac{P_0}{z_0} \tag{5.28}$$

Modeled values match Krypton at a pressure of 60 mbar and a temperature of 300K. Experimental measurements with these settings are discussed in depth in the gas permeation results section.

5.6.2 Simulation results

Figure 5.3 shows the bode plot and analogous real-imaginary graph with the simulation results. The simulation has been run using the values listed in table 5.1. Amplification is chosen such that the magnitude lies close to 0 dB in the circuit. The mechanical resonance is clearly visible on the right in all three graphs. In the imaginary part of the graph two bumps are visible. These bumps correspond to the two time constants τ_{gas} and τ_{th}. The two time constants are easiest seen in the real-imaginary graph, which is why this representation is used in the following chapters.

The modeled data are fitted to the algebraic expression in equation 5.4. The fitting should return the values that were used as an input to the model:

$$\tau_{th} = R_{th}C_{th} = 35 \text{ ns}$$
$$\tau_{gas} = R_{gas}C_{gas} = 804 \text{ ns}$$

A fit to the simulated data is shown in figure 5.4. The fitted value for τ_{gas}, 806 ns, matches the modeled value of 804 ns. On the other hand, the thermal equilibration time τ_{th} matches significantly worse. Fitting results in a time constant of 30 ns, which is 15% away from the modeled value. It is asserted that the proximity of the resonance peak has a negative impact on the quality of the fit, since the algebraic expression does not include the resonance peak.

In order to improve data analysis, a Laplacian is fitted to the resonance peak in panel A and subtracted to arrive at the result in panel B. Then, the original fitting procedure to find the two time constants is applied. New τ_{th} and τ_{gas} found are respectively 36 and 780 ns. Both values are within 3% from modeled. It turns out that subtracting the resonance peak greatly improves the results for the thermal time constant, and slightly affects the permeation time constant.

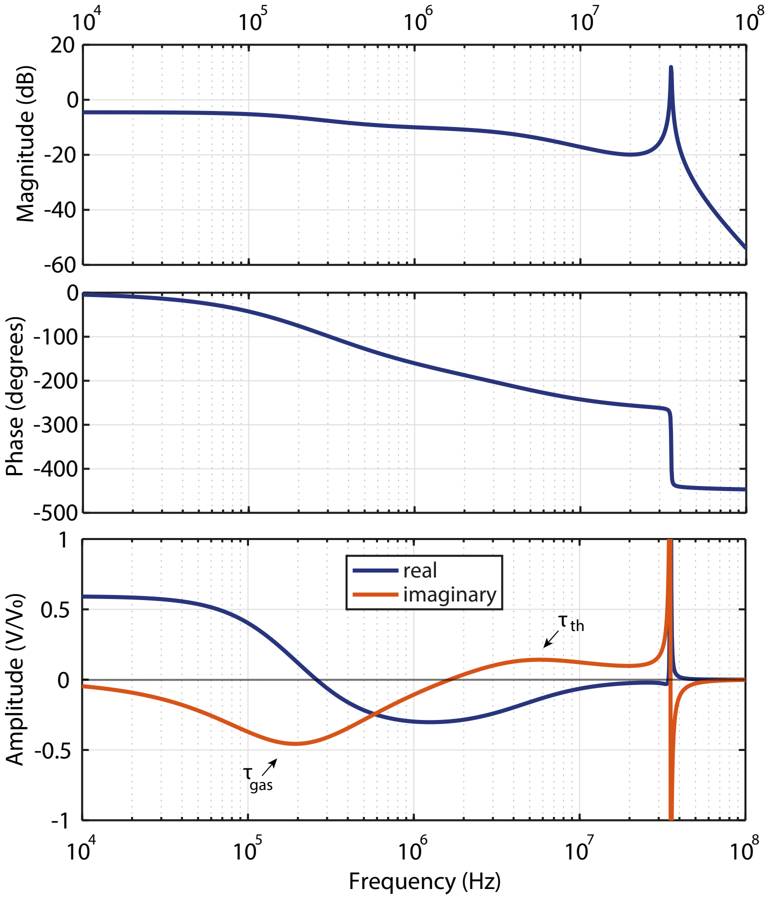

Figure 5.3: Simulated results using an equivalent electric circuit for the porous membrane, represented in a magnitude plot, a phase plot and a real-imaginary plot. The mechanical resonance at 35 MHz is pronounced in all three graphs. The two time constants τ_{gas} and τ_{th} are recognizable as two bumps in the graph of the imaginary part.

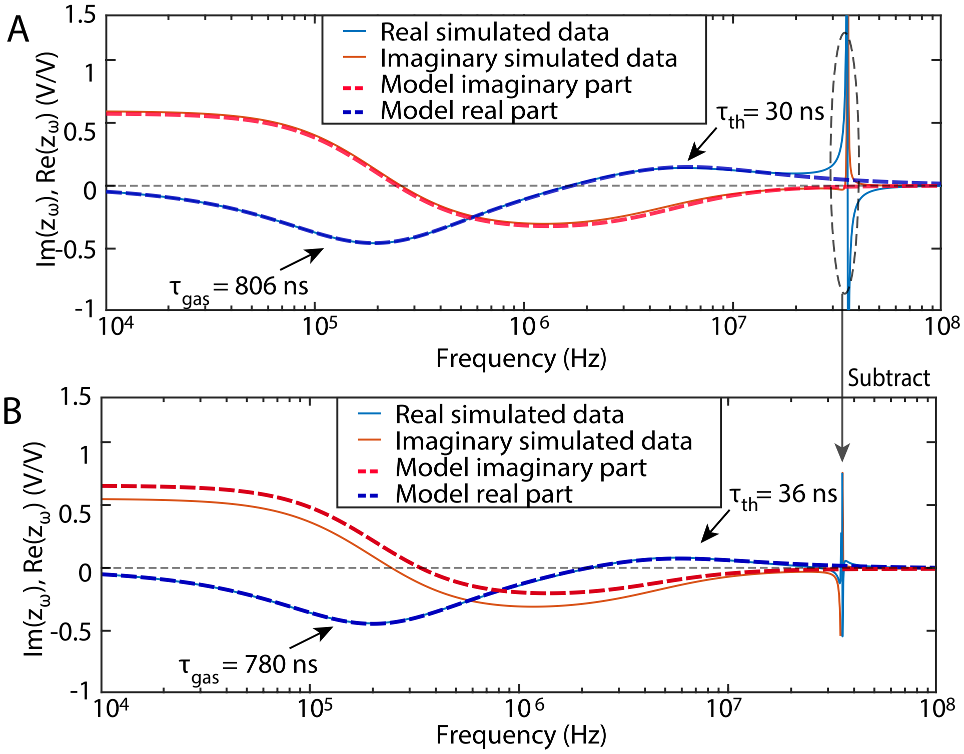

Figure 5.4: Simulated results are fitted to the algebraic model in equation 5.4. A) Fit to original simulated data with fitted parameters $a = 0.36$, $b = 0.94$, $\tau_{th} = 30$ ns and $\tau_{gas} = 806$ ns. B) A harmonic oscillator response with $f_0 = 35$ MHz and $Q = 51$ is subtracted to improve fitting. The new fitted parameters are: $a = 0.27$, $b = 0.95$, $\tau_{th} = 36$ ns and $\tau_{gas} = 780$ ns.

6 RESULTS

This chapter discusses the gas permeation measurements of two porous graphene samples. The samples in this chapter have been exposed to highly energetic ion bombardment with $136Xe^{42+}6.6MeV/u$, with a fluence of $5.09 \cdot 10^9$ ions per square centimeter at the SME beamline of GANIL (Caen, France), which is similar to the treatment described by Madauß et al.[20]

The reader is first introduced to the typical form of a frequency response that is obtained from the experiments. Then, it is argued that the measured results can be explained by the model proposed in chapter 5. To verify the model the gas permeation time constants are extracted and shown to follow Graham's effusion law with $\tau_{gas} \propto \sqrt{M}$. Also the dependency of the thermal time constants on the gas is discussed. The presence of gas opens a new thermal pathway, decreasing the time needed for transfer of energy. Measurement sets of two drums are discussed in depth.

6.1 TYPICAL RESPONSE

A typical frequency response including both phase delays and the first mechanical resonance peak is displayed in figure 6.1. Both the real and imaginary parts of the data are shown. As the first mechanical resonance at 22.1 MHz obscures a part of data of interest, a fit to the resonance is subtracted from the data in figure 6.1A to obtain the graph in figure 6.1B. Now, it is possible to fit the imaginary part of the data in panel B. The imaginary part of the response has two clear bumps. These bumps correspond to the two time constants τ_{gas} and τ_{th}, as indicated in the figure. The observed real part of the amplitude is slightly offset along all frequencies, probably due to cross-talk between the red and blue laser.

6.1.1 Time constants

The two bumps in the imaginary part of the frequency response are caused by phase delay with respect to the applied optothermal drive of either the pressure inside the cavity or the temperature of the membrane. The observed behavior can be summarized as follows:

- $\omega << \tau_{gas}, \tau_{th}, \omega_0$: In the low-frequency limit the motion of the membrane follows the applied drive and the response is purely real.
- $\omega \approx \tau_{gas}$: At frequencies close to the associated permeation time constant $\tau_{gas} = 1/\omega$ the pressure of the gas trapped inside the cavity is out of phase with respect to the movement of the membrane. This results in membrane motion being out of phase with respect to the drive caused by gas actuation.

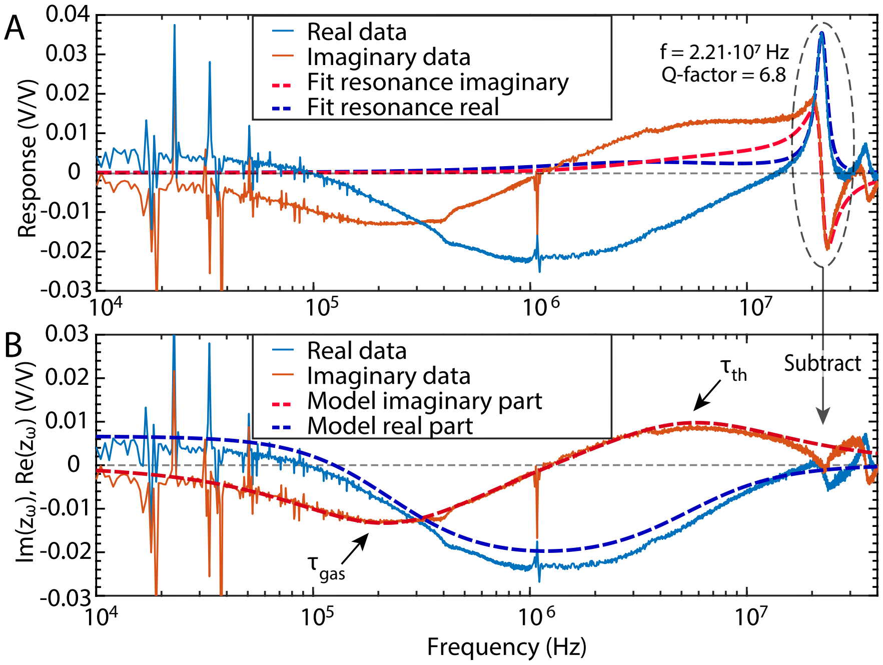

Figure 6.1: Frequency response of the drum in Krypton at 60 mbar. In A the original response including the mechanical resonance peak at 22 MHz is shown. The harmonic oscillator fits (shown in A) are subtracted to arrive at B. Now, the model with two time constants can be applied with fitted parameters $a = 0.017$, $b = 0.019$, $\tau_{th} = 35$ ns and $\tau_{gas} = 805$ ns.

- $\omega \approx \tau_{th}$: At frequencies close to the associated thermal time constant $\tau_{th} = 1/\omega$ the membrane temperature is out of phase with respect to the movement of the membrane. This again results in membrane motion being out of phase with respect to the drive.
- $\omega \approx \omega_0$: At a driving frequency close to the mechanical resonance a resonance peak appears independently of the pneumatic and thermal delays.

6.1.2 Coefficients

The coefficients a and b set the peak heights of the two bumps. The sign of coefficient a can be either positive or negative depending on the buckling direction of the membrane. The buckling direction determines whether a tension increase causes the membrane to move towards or away from the substrate. The parameter b will always have the same sign, as the forces from the gas act independently from the membrane buckling. The opposite signs for the two coefficients are favorable in sight of data analysis, as it is easier to distinguish the two bumps when they have opposite direction.

6.2 MEASUREMENTS

The permeation and thermal time constants τ_{gas} and τ_{th} are extracted for a range of gasses varying in mass from 4u (He) to 130u (SF_6). The experimental results from two devices are presented in figures 6.2 and 6.3. Each figure presents a series of measurements performed at 60 mbar in panel A. Panel B and C show permeation and thermal time constants at all various pressures including the measurements in panel A. The results from the two samples are discussed separately.

SAMPLE 1 Panel A in figure 6.2 presents a series of measurements at 60 mbar with different gasses, where the molecular mass of each gas is indicated by a circle. The effusion time clearly depends on the mass of the gas, shifting to lower frequencies with increasing mass. The imaginary part of the measurement data is fitted (grey lines) to equation (5.4) and both time constants are marked by red bars. While τ_{gas} varies nearly an order of magnitude, the thermal time τ_{th} is almost constant. Panel B shows that the permeation time constant closely follows Graham's effusion law with $\tau_{gas} \propto \sqrt{M}$. This agrees with equation 2.12 for classical effusion. At a pressure of 500 mbar $Kn < 1$ for only SF_6. At 1000 mbar all gasses except Helium and Neon have $Kn < 1$. The behavior in the environments with low Knudsen number deviates from the effusion trend that is visible at the higher Knudsen numbers. The viscosity of the gas starts playing a role and the measurements no longer coincide with the line drawn for the effusion model.

SAMPLE 2 Panel A in figure 6.3 presents a series of measurements at 60 mbar with different gasses, where the molecular mass of each gas is indicated by a circle. The measurements on tetrafluormethane and sulfurhexafluoride differ from the trend visible along the other gasses. These two gasses have been measured separately, a week later. The change could be explained by experimental mistakes or sample degradation during the week. The imaginary part of the measurement data is fitted (grey lines) to equation (5.4) and both time constants are marked by red bars. Panel B shows that the permeation time constant follows Graham's effusion law $\tau_{gas} \propto \sqrt{M}$ when tetrafluormethane and sulfurhexafluoride are not taken into account. At a pressure of 500 mbar $Kn < 1$ for only SF_6. At 1000 mbar all gasses except Helium and Neon have $Kn < 1$. The behavior in the environments with low Knudsen number deviates from the effusion trend that is visible at the higher Knudsen numbers. The viscosity of the gas starts playing a role and the measurements no longer coincide with the line drawn for the effusion model.

6.3 THERMAL TIME CONSTANT

The presence of gas in the cavity opens a new thermal pathway for the membrane to lose heat and the thermal time constant is expected to decrease as compared to the vacuum measurement. In view of the small dimensions of the gap between the membrane and the substrate the Knudsen formula is used to calculate the effective thermal conductivity k_{eff} of the gas:

$$\frac{k_{eff}}{k_0} = \frac{1}{1 + \frac{CT}{Pd}} \tag{6.1}$$

Where C is a constant equal to $7.6 * 10^{-5}$, d is the distance between the membrane and the substrate and k_0 is the thermal conductivity of the gas.[52,53] Panel B in figures 6.2 and 6.3 show that the gas indeed provides a new heat

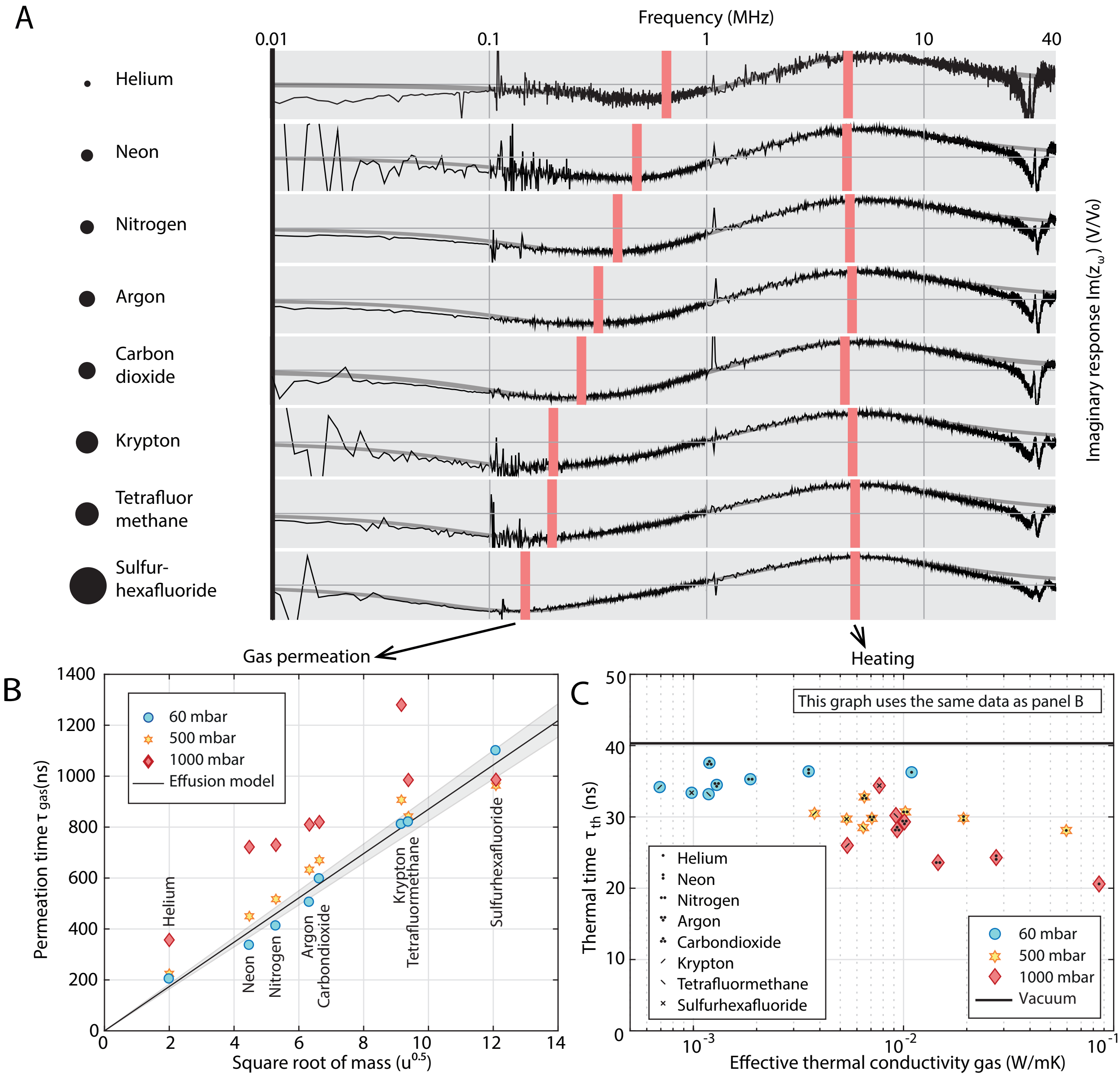

Figure 6.2: Measured permeation and heating times of a porous SLG membrane for various gasses. In panel A the imaginary part of the signal is overlayed by its fit and the extracted time constant are highlighted by red marks for measurements performed at 60 mbar. The gray bounds represent a response of 0.04 V/V_0. The relative particle mass is represented by the area of the circles next to the gas name. Panel B shows that the permeation time τ_{gas} follows the square root of the particle mass according to equation 2.12. At higher pressures the Knudsen number becomes too low for classical effusion to apply and the measurements deviate from this law. Panel C shows the thermal time τ_{th} as compared to a measurement in vacuum.

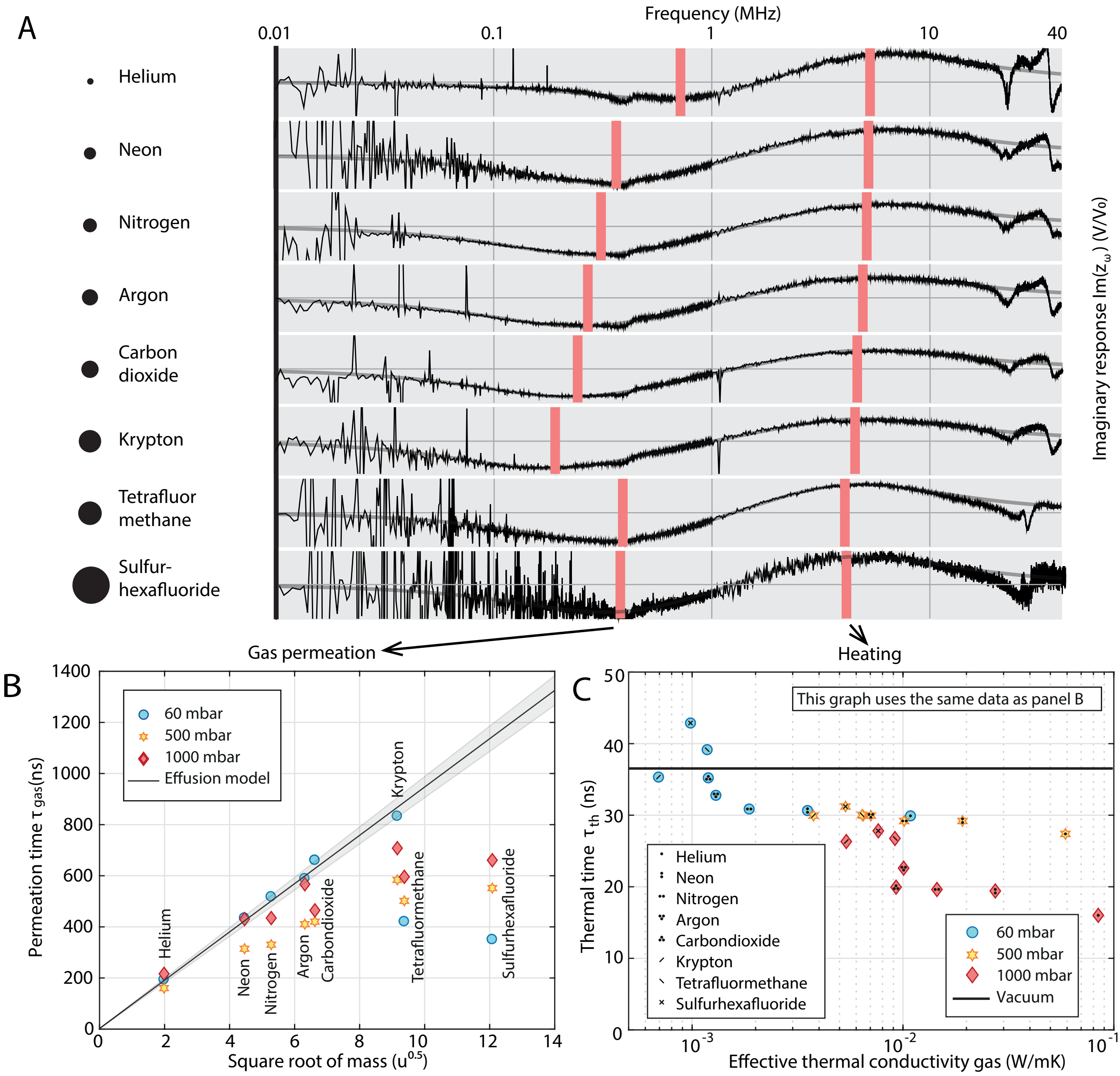

Figure 6.3: Measured permeation and heating times of a porous SLG membrane for various gasses. In panel A the imaginary part of the signal is overlayed by its fit and the extracted time constant are highlighted by red marks for measurements performed at 60 mbar. The gray bounds represent a response of 0.04 V/V_0. The relative particle mass is represented by the area of the circles next to the gas name. Panel B shows that the permeation time τ_{gas} follows the square root of the particle mass according to equation 2.12. At higher pressures the Knudsen number becomes too low for classical effusion to apply and the measurements deviate from this law. Panel C shows the thermal time τ_{th} as compared to a measurement in vacuum.

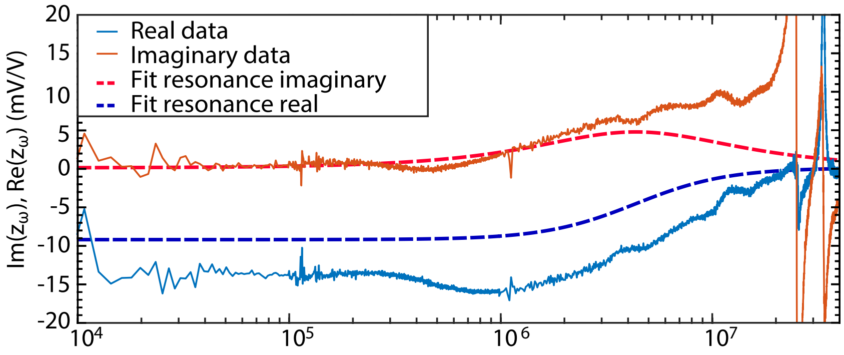

Figure 6.4: Frequency response of a perforated drum at a pressure of 8 mbar, which is considered low vacuum. The original response including two mechanical resonance peaks is shown. The harmonic oscillator fits for the first resonance (not shown) are subtracted before further analysis. A model with only thermal delay can be applied with fitted parameters $a = 0.0023$, $\tau_{th} = 36$ ns, $f = 25.5$ MHz and $q = 31$.

conduction pathway, decreasing the thermal time constant as the effective thermal conductivity increases.

6.4 COMPARISON WITH VACUUM

The presence of two time constants is characteristic for perforated membranes in gaseous environments. Measurements in vacuum show only one maximum in the imaginary response, corresponding to a thermal time $\tau_{th} =$ 41 ns for sample 1 and $\tau_{th} = 36$ ns for sample 2. Figure 6.4 shows a frequency response of a perforated drum at low vacuum. The first bump, attributable to the permeation delay, diminishes. The thermal delay with $\tau_{th} = 36$ns is still present. Also, the unperforated reference samples show only one peak, again corresponding to expected values for τ_{th}. Therefore, it has to be concluded that the measured response indeed must be a contribution of gas permeation.

7 CONCLUSION AND DISCUSSION

A sensing method is presented that is based on measuring the phase delay of the membrane motion caused by the forces from the permeating gas. Perforations allow the gas to flow out at a speed characteristic for the gas species. At driving frequencies close to the corresponding permeation speed, the membrane's phase delay is maximal. The method is well able to distinguish gasses with varying mass based on their effusion speed.

In this thesis two samples are highlighted. These samples have both small pores which are 14 nm on average and a single big pore of approximately 400 nm. The big pore size lies within the Knudsen effusion regime and permeation time constant are shown to follow Graham's law with $\tau_{gas} \propto \sqrt{M}$ for measurements on a range of gasses (He, Ne, N_2, Ar, CO_2, Kr, CH_4 and SF_6) at a pressure of 60 mbar. At increased pressures of 500 and 1000 mbar the behavior deviates from Graham's law whenever $Kn < 1$. The permeation rate measurements seemingly benefit from the big pore by the increased response arising from the high flow.

This research explains the mechanical behavior of a perforated resonator below its resonance frequency in the presence of gas. The measurement of the frequency response curve performs well at frequencies down to 10 kHz. The method is less suitable for lower frequencies and corresponding low permeation speeds, at which colorimetry or capacitive read-out are more suitable. Phase delay gas recognition opens a new, higher detection range of over 3 orders of magnitude.

7.1 GAS PERMEATION MODEL

The measured frequency response is explained by a gas permeation model which describes the mechanical response to a sinusoidal driving force of a perforated graphene membrane in gaseous environment. It is argued that two delays are present in the frequency response below the first mechanical resonance. The delays depend on the characteristic gas permeation time τ_{gas} and the thermal equilibration time τ_{th}. The gas permeation model is tested by simulation of an equivalent circuit in Simulink. The simulations verify that two permeation time constants can be seen below the first mechanical resonance. Further improvements can be made to achieve a model that is more versatile, including squeeze film and gas damping effects.

In the mechanical domain the values of the resonance frequency and Q-factor are predefined before running the simulation. Therefore, the model does not calculate effects as gas damping and squeeze film stiffness increase. Implementation would require automatic numerical value calculation of the electrical components, based on gas, pressure and temperature input. This would also greatly enhance the ease of use of the simulation.

The presented model is applicable not only for graphene but to any two-dimensional material, provided that it can be optothermally driven. The permeability of the pores can be tuned by changing the size and chemical structure to achieve specific response, allowing for far higher sensitivities. The inherent high measurement speed of the method and low power consumption promise implementability as a gas, chemical and biological sensor for portable devices.

7.2 RECOMMENDATIONS

Hundreds of drums perforated with only small pores have been checked, but finding the characteristic behavior with two time constants proved to be very hard. Three drums have been found to show this behavior. Two of them have been characterized using the AFM and turned out to have a big hole in them, which increased the effusion area by a factor two.

The presence of both small pores and a big pore gives space to questions about the exact permeation pathway. It is therefore recommendable to rule out the possibility that the gas is escaping only through the big pore. An additional measurement with a milled big pore in an otherwise unperforated membrane should clarify this matter. It is suggested to perform the milling with a focused ion beam for controllable pore size or use samples with a venting channel.

The most interesting applications of nanoporous graphene require downsizing the pores even farther. To assure reasonable sensitivities a high porosity is needed. Therefore, it is recommended to work with higher porosities than presented in this work. Nevertheless, this thesis shows an account of MEMS gas sensing on timescales not accessible before. The understanding of the interplay between the gas and the membrane mechanics makes it possible to predict mechanical phase delay in nanodrum oscillators and paves the way to broader application of two-dimensional materials.

BIBLIOGRAPHY

[1] Meyer, J. C.; Geim, A. K.; Katsnelson, M. I.; Novoselov, K. S.; Booth, T. J.; Roth, S. *Nature* **2007**, *446*, 60.

[2] of Sciences, T. R. S. A. Scientifc Background on the Nobel Prize in Physics 2010 Graphene. 2010.

[3] Cheng, Z.; Li, Q.; Li, Z.; Zhou, Q.; Fang, Y. *Nano letters* **2010**, *10*, 1864–1868.

[4] Leenaerts, O.; Partoens, B.; Peeters, F. *Applied Physics Letters* **2008**, *93*, 193107.

[5] Han, T. H.; Huang, Y.-K.; Tan, A. T.; Dravid, V. P.; Huang, J. *Journal of the American Chemical Society* **2011**, *133*, 15264–15267.

[6] Cohen-Tanugi, D.; Grossman, J. C. *Nano letters* **2012**, *12*, 3602–3608.

[7] Joshi, R.; Carbone, P.; Wang, F.-C.; Kravets, V. G.; Su, Y.; Grigorieva, I. V.; Wu, H.; Geim, A. K.; Nair, R. R. *science* **2014**, *343*, 752–754.

[8] Celebi, K.; Buchheim, J.; Wyss, R. M.; Droudian, A.; Gasser, P.; Shorubalko, I.; Kye, J.-I.; Lee, C.; Park, H. G. *Science* **2014**, *344*, 289–292.

[9] Zeng, J.; Liu, J.; Yao, H.; Zhai, P.; Zhang, S.; Guo, H.; Hu, P.; Duan, J.; Mo, D.; Hou, M. *Carbon* **2016**, *100*, 16–26.

[10] Sint, K.; Wang, B.; Král, P. *Journal of the American Chemical Society* **2008**, *130*, 16448–16449.

[11] Wang, T.; Huang, D.; Yang, Z.; Xu, S.; He, G.; Li, X.; Hu, N.; Yin, G.; He, D.; Zhang, L. *Nano-Micro Letters* **2016**, *8*, 95–119.

[12] Robert, P.; Nguyen, V.; Hentz, S.; Duraffourg, L.; Jourdan, G.; Arcamone, J.; Harrisson, S. MEMS and NEMS: A new approach for ultra-low cost 3D inertial sensor. Sensors, 2009 IEEE. 2009; pp 963–966.

[13] Jensen, K.; Kim, K.; Zettl, A. *Nature nanotechnology* **2008**, *3*, 533.

[14] Dolleman, R. J.; Davidovikj, D.; Cartamil-Bueno, S. J.; van der Zant, H. S.; Steeneken, P. G. *Nano letters* **2016**, *16*, 568–571.

[15] Fang, Z.; Liu, Z.; Wang, Y.; Ajayan, P. M.; Nordlander, P.; Halas, N. J. *Nano letters* **2012**, *12*, 3808–3813.

[16] Robinson, J. T.; Zalalutdinov, M.; Baldwin, J. W.; Snow, E. S.; Wei, Z.; Sheehan, P.; Houston, B. H. *Nano letters* **2008**, *8*, 3441–3445.

[17] Davidovikj, D.; Slim, J. J.; Cartamil-Bueno, S. J.; van der Zant, H. S.; Steeneken, P. G.; Venstra, W. J. *Nano letters* **2016**, *16*, 2768–2773.

[18] Cartamil Bueno, S. *Freestanding 2D Materials and their Applications*; Doctoral thesis, 2017.

[19] De Alba, R.; Massel, F.; Storch, I. R.; Abhilash, T.; Hui, A.; McEuen, P. L.; Craighead, H. G.; Parpia, J. M. *Nature nanotechnology* **2016**, *11*, 741.

[20] Madauß, L.; Schumacher, J.; Ghosh, M.; Ochedowski, O.; Meyer, J.; Lebius, H.; Ban-d'Etat, B.; Toimil-Molares, M. E.; Trautmann, C.; Lammertink, R. *Nanoscale* **2017**, *9*, 10487–10493.

[21] Li, H.; Song, Z.; Zhang, X.; Huang, Y.; Li, S.; Mao, Y.; Ploehn, H. J.; Bao, Y.; Yu, M. *Science* **2013**, *342*, 95–98.

[22] Koenig, S. P.; Wang, L.; Pellegrino, J.; Bunch, J. S. *Nature nanotechnology* **2012**, *7*, 728.

[23] Hooke, R. *Lectiones Cutlerianae: or A collection of lectures: physical, mechanical, geographical, & astronomical*; John Martyn London, 1679.

[24] Newton, I.; Machin, J. *The Mathematical Principles of Natural Philosophy*; 1729.

[25] Wolfson, R. *Essential University Physics: Pearson New International Edition*; Pearson Higher Ed, 2013; Vol. 1.

[26] Griffiths, D. J. *Introduction to electrodynamics*; Prentice Hall, 1962.

[27] Zener, C. *Physical review* **1937**, *52*, 230.

[28] Sun, Y.; Fang, D.; Soh, A. K. *International Journal of Solids and Structures* **2006**, *43*, 3213–3229.

[29] Bömmel, H.; Dransfeld, K. *Physical Review* **1960**, *117*, 1245.

[30] Kunal, K.; Aluru, N. *Physical Review B* **2011**, *84*, 245450.

[31] Duan, K.; Li, L.; Hu, Y.; Wang, X. *Materials & Design* **2017**, *133*, 455–463.

[32] Robinson, J. T.; Zalalutdinov, M. K.; Cress, C. D.; Culbertson, J. C.; Friedman, A. L.; Merrill, A.; Landi, B. J. *ACS nano* **2017**, *11*, 4745–4752.

[33] Liu, Y.; Chen, X. *Journal of Applied Physics* **2014**, *115*, 034303.

[34] Cohen-Tanugi, D.; Grossman, J. C. *Nano letters* **2014**, *14*, 6171–6178.

[35] Unterreithmeier, Q. P.; Faust, T.; Kotthaus, J. P. *Physical review letters* **2010**, *105*, 027205.

[36] Grantab, R.; Shenoy, V. B.; Ruoff, R. S. *Science* **2010**, *330*, 946–948.

[37] Wei, Y.; Wu, J.; Yin, H.; Shi, X.; Yang, R.; Dresselhaus, M. *Nature materials* **2012**, *11*, 759.

[38] Lee, G. H.; Cooper, R. C.; An, S. J.; Lee, S.; van der Zande, A.; Petrone, N.; Hammerberg, A. G.; Lee, C.; Crawford, B.; Oliver, W. *Science* **2013**, *340*, 1073–1076.

[39] Sharipov, F. *Rarefied gas dynamics: fundamentals for research and practice*; John Wiley & Sons, 2015.

[40] Boutilier, M. S.; Hadjiconstantinou, N. G.; Karnik, R. *Nanotechnology* **2017**, *28*, 184003.

[41] Gruener, S.; Huber, P. *Physical review letters* **2008**, *100*, 064502.

[42] Sampson, R. A. *Philosophical Transactions of the Royal Society of London. A* **1891**, *182*, 449–518.

[43] Tan, Z. *Air Pollution and Greenhouse Gases*; Springer, 2014; pp 27–58.

[44] Drahushuk, L. W.; Strano, M. S. *Langmuir* **2012**, *28*, 16671–16678.

[45] Du, H.; Li, J.; Zhang, J.; Su, G.; Li, X.; Zhao, Y. *The Journal of Physical Chemistry C* **2011**, *115*, 23261–23266.

[46] Bonaccorso, F.; Sun, Z.; Hasan, T.; Ferrari, A. *Nature photonics* **2010**, *4*, 611.

[47] Davidovikj, D. *Two-dimensional membranes in motion*; Doctoral thesis, 2018.

[48] Deng, S.; Berry, V. *Materials Today* **2016**, *19*, 197–212.

[49] Compton, O. C.; Nguyen, S. T. *small* **2010**, *6*, 711–723.

[50] Zhu, W.; Low, T.; Perebeinos, V.; Bol, A. A.; Zhu, Y.; Yan, H.; Tersoff, J.; Avouris, P. *Nano letters* **2012**, *12*, 3431–3436.

[51] Balandin, A. A.; Ghosh, S.; Bao, W.; Calizo, I.; Teweldebrhan, D.; Miao, F.; Lau, C. N. *Nano letters* **2008**, *8*, 902–907.

[52] Reichenauer, G.; Heinemann, U.; Ebert, H.-P. *Colloids and Surfaces A: Physicochemical and Engineering Aspects* **2007**, *300*, 204–210.

[53] Antonetti, V.; Bar Cohen, A.; Bergles, A. *Fluid Flow Databook*; Genium Publishing, 1981; Chapter 410.2.

[54] Marcia, H. L.; Allan, H. H. *Thermal Conductivity of Gases*; CRC-Press, Boca Raton, FL, 2011.

[55] ToolBox, E. Specific Heat and Individual Gas Constant of Gases. 2003; `https://www.engineeringtoolbox.com/specific-heat-capacity-gases-d_159.html`.

A TABLES

Table A.1: Gas properties of gasses used during the experiments.[54,55]

	Kinetic diameter (10^{-10} m)	Mass (u)	Specific heat capacity (J/KgK)	Thermal conductivity (10^{-3} W/mK)
Nitrogen	3.6	28	1047	26
Neon	2.8	20	1038	49
Krypton	3.6	84	251	10
Helium	2.6	4	5204	150
Argon	3.4	40	532	18
Carbondioxide	3.3	44	837	16
Sulfurhexafluoride	5.5	146	669	14
Tetrafluorcarbon	4.7	88	658	16

Table A.2: Mean free path (mfp) and Knudsen number (Kn) for the gasses used in the experiments at various pressures assuming a 400 nm pore.

	1000 mbar		500 mbar		60 mbar	
	mfp (nm)	Kn	mfp (nm)	Kn	mfp (nm)	Kn
Nitrogen	220	0.6	440	1.1	3700	9
Neon	390	1.0	780	1.9	6500	16
Krypton	230	0.6	450	1.1	3800	9
Helium	430	1.1	870	2.2	7200	18
Argon	250	0.6	510	1.3	4200	11
Carbondioxide	270	0.7	540	1.3	4500	11
Sulfurhexafluoride	970	0.2	200	0.5	1600	4
Tetrafluorcarbon	130	0.3	270	0.7	2200	6

COLOPHON

This document was typeset using LaTeX. The document layout was generated using the `arsclassica` package by Lorenzo Pantieri, which is an adaption of the original `classicthesis` package from André Miede.